Energy Conversion and Management 304 (2024) 118233

Contents lists available at ScienceDirect

Energy Conversion and Management

journal homepage: www.elsevier.com/locate/enconman

Research paper

# Adiabatic Compressed Air Energy Storage system performance with application-oriented designed axial-flow compressor

Daniel L. Pottie [a,*], Maury M. Oliveira Jr [a], Bruno Cardenas [b], Zahra Baniamerian [b], Seamus Garvey [b], James Rouse [b], Edward Hough [c], Audrius Bagdanavicius [d], Abdullah M. Ali [d], Philip Eames [a], Edward R. Barbour [a]

[a] Centre for Renewable Energy System Technology (CREST), Loughborough University, Loughborough, LE11 3TU, UK
[b] Faculty of Engineering, University of Nottingham, Nottingham, NG7 2RD, UK
[c] British Geological Survey, Nottingham, NG12 5GG, UK
[d] School of Engineering, University of Leicester, Leicester, LE1 7RH, UK

ARTICLE INFO

*Keywords:*
ACAES
Axial-flow compressor
Throughflow method
Energy storage
Thermo-mechanical energy storage

ABSTRACT

Medium and long-duration energy storage systems are expected to play a critical role in the transition towards electrical grids powered by renewable energy sources. ACAES is a promising solution, capable of handling power and energy ratings over hundreds of MW and MWh, respectively. One challenge with ACAES is achieving the required highly efficient operation in the compressor over the range of conditions encountered in the system as the pressure in the air store changes. In this paper, an application-oriented axial-flow compressor is designed, aiming towards efficient operation throughout the operation range, whilst also associating the performance prediction to a practical compressor geometry. A two-step design methodology based on inviscid, axisymmetric flow conditions has been implemented, leading to the flowtrack, blade-row geometries and the compressor performance map. The compressor model is integrated into an ACAES model, including two compression spools, two expansion stages with preheat, a constant volume high pressure storage operating between 5.5 and 7.7 MPa and two separate Thermal Energy Storage units. While the existing ACAES literature either ignores the transient off-design operation or uses generic numerical correlations (which are not associated to a particular geometry), the key novelty of this paper is the application of a detailed design method for turbomachinery to ACAES. The results indicate that the designed compressor requires 33 stages over the two spools, and is able to operate efficiently over the storage pressure range, showing that if the application-oriented design procedure is applied to the compressor, it does not stop ACAES reaching 70% round-trip efficiency, outputting 35MW for approximately 15 h. Importantly, the specific ACAES requirement of conserving heat at higher temperatures has been fulfilled by decreasing the number of intercoolers. Finally, it is recommended that a similar level of scrutiny is applied to the other components (*i.e.* expanders, heat exchangers and TES units), keeping in mind the unique set of operational requirements of ACAES. This work is an important step towards removing the common misconception that off-the-shelf components can be easily be used in typical ACAES designs.

## 1. Introduction

Successful deployment of medium (between 4 and 200 h [1]) and long duration (over 200 h) energy storage systems is integral in enabling net-zero in most countries. Despite the urgency of extensive implementation, practical large-scale storage besides Pumped Hydro (PHES) remains elusive [2]. Within the set of proposed alternatives to PHES, Adiabatic Compressed Air Energy Storage (ACAES) has long been regarded a promising technology capable of storing ⩾100's MWh, at discharging periods generally greater than eight hours and power ratings over 100's MW [3]. ACAES is regarded as a technology capable of performing energy arbitrage, peak shaving, infrastructure upgrade deferral, black-start, and even demand-response limited [4]. Research interest in ACAES systems has grown steadily over the past two decades [5], with most publications consisting of numerical thermodynamic analysis, occasionally supported by part-plant experiments [6].

The working principle of ACAES is as follows: Surplus power from the grid (or, alternatively, directly from renewable energy sources RES such as wave-powered [7], photovoltaic [8] or wind [9]) is used to

* Corresponding author.
*E-mail address:* D.L.Pottie@lboro.ac.uk (D.L. Pottie).

https://doi.org/10.1016/j.enconman.2024.118233
Received 26 October 2023; Received in revised form 2 February 2024; Accepted 19 February 2024
Available online 27 February 2024

## Nomenclature

### Symbols

| | |
|---|---|
| $+m$ | Streamwise direction, |
| $+n$ | Normal direction, |
| $+r$ | Radial direction, |
| $+y$ | *Quasi-normal* direction, |
| $+z$ | Axial direction, |
| $A$ | Area, $m^2$, |
| $\vec{C}$ | Absolute velocity (vector), m $s^{-1}$, |
| $C$ | Absolute velocity (scalar), m $s^{-1}$, |
| $\mathbb{C}$ | Blade chord length, m, |
| $C_{D,s}$ | Howell modified drag coefficient, |
| $C_L$ | Lift Coefficient, |
| $c_p$ | Specific heat at constant pressure, J $kg^{-1}$ $K^{-1}$, |
| $C_r$ | Heat capacity ratio, |
| $DF$ | Diffusion Factor, |
| $DF_{EQ}$ | Lieblein's Equivalent Diffusion Factor, |
| $\mathbb{H}$ | Blade height, m |
| $h$ | Specific enthalpy, J $kg^{-1}$, |
| $i$ | Station index, |
| $I$ | Rothalpy, J $kg^{-1}$ |
| $L_{\dot{m}}$ | Number of mass flow rate off-design conditions tested, |
| $L_{\omega}$ | Number of rotational speed off-design conditions tested, |
| $m$ | Streamwise coordinate, m, |
| $\dot{m}$ | Mass flow rate, kg $s^{-1}$, |
| $Ma$ | Mach number, |
| $\mathcal{N}$ | Number of nodes along a *quasi-normal* |
| $P$ | Pressure, Pa |
| $\mathcal{R}$ | Degree of reaction, |
| $r$ | Radial position/coordinate, m |
| $S$ | Number of stations on a spool, |
| $SS$ | Speed of sound, m $s^{-1}$, |
| $s$ | Specific entropy, J $kg^{-1}$ $K^{-1}$, |
| $\mathbb{S}(r)$ | Local pitch, m, |
| $sg$ | Stage index, |
| $\vec{U}$ | Blade tangential velocity (vector), m $s^{-1}$, |
| $T$ | Temperature, K, |
| $\mathbb{T}$ | Blade thickness, m |
| $t$ | Time, s, |
| $u$ | Specific internal energy, J $kg^{-1}$, |
| $U$ | Blade tangential velocity (scalar), m $s^{-1}$, |
| $\vec{V}$ | Relative velocity (vector), m $s^{-1}$, |
| $V$ | Relative velocity (scalar), m $s^{-1}$, |
| $\dot{W}$ | Work (power), J, |
| $\Delta w$ | Specific work, J $kg^{-1}$, |
| $y$ | *Quasi-normal* coordinate, |

### Greek Characters

| | |
|---|---|
| $+\theta$ | Tangential direction, |
| $\alpha$ | Absolute flow angle, |
| $\beta$ | Relative flow angle, |
| $\gamma_s$ | Stagger angle, |
| $\delta$ | Deviation angle, |
| $\delta\epsilon$ | Flow turning departure, $\lvert\epsilon^{OFF} - \epsilon^{ON}\rvert$, |
| $\delta\imath$ | Incidence angle departure, $\lvert\imath^{OFF} - \imath^{ON}\rvert$, |
| $\varepsilon$ | Heat exchanger effectiveness, |
| $\zeta_P$ | Pressure loss coefficient, |
| $\zeta_1$ | Primary loss coefficient, |
| $\zeta_2$ | Secondary loss coefficient, |
| $\zeta_{ew}$ | End-wall loss coefficient, |
| $\eta$ | Efficiency, |
| $\theta$ | Blade camber angle, |
| $\imath$ | Incidence angle, |
| $\kappa$ | Curvature, $m^{-1}$, |
| $\Lambda$ | Blade aspect ratio, |
| $\rho$ | Density, kg $m^{-3}$, |
| $\sigma$ | Blade solidity, |
| $\phi$ | Stream surface angle, |
| $\varphi$ | Flow coefficient, |
| $\psi$ | Load coefficient, |
| $\vec{\omega}$ | Rotational speed (vector), $s^{-1}$, |
| $\omega$ | Rotational speed (scalar), $s^{-1}$, |

### Subscripts

| | |
|---|---|
| $\emptyset$ | Absolute stagnation property, |
| $\emptyset R$ | Relative stagnation property, |
| 1 | Relative to the rotor inlet (station 1) |
| 2 | Relative to the rotor outlet/stator inlet (station 2) |
| 3 | Relative to the stator outlet (station 3) |
| $a$ | Ambient condition, |
| $AC$ | Corresponding to the after-cooler heat exchanger, |
| $air$ | Air property, |
| $c$ | Compressor, |
| $chg$ | Relative to the charging process, |
| $C_\theta$ | Relative to the absolute tangential velocity, |
| $cool$ | Coolant property, |
| $dis$ | Relative to the discharging process, |
| $e$ | Expander, |
| $ew$ | End-wall, |
| $hub$ | Relative to the hub radius, |
| $HPST$ | Property evaluated at the High-pressure Storage, |
| $IC$ | Corresponding to the inter-cooler heat exchanger, |
| $idle$ | Corresponding to the idle period, |
| $in$ | Property evaluated at the blade row inlet, |
| $m$ | Component in the streamwise direction, |
| $N$ | Condition evaluated at the node N, |
| $n$ | Component in the normal direction, |
| $R$ | Relative to the rotating blades (rotors), |

drive compressors which intake atmospheric air. Upon leaving the compressors, the exergy in the hot pressurised air is divided into its pressure and temperature components in heat exchangers. The air is stored in a high-pressure store (HPST) and the heat in a separate thermal energy store (TES). When there is a grid net demand, the ACAES system discharges by releasing the compressed air from the HPST, recombining it in heat exchangers with the thermal energy stored in the TES. The hot pressurised air is then expanded in turbines, which drive electrical generators [3]. The key difference between ACAES and its technological

| | |
|---|---|
| $rec$ | Relative to the recovery period, |
| $ref$ | Reference radius, |
| $S$ | Relative to the static blades (stators and guide vanes), |
| $SP_n$ | Relative to the $n$th compressor spool, |
| $SS$ | Relative to a streamsheet, |
| $tip$ | Relative to the tip radius, |
| $z$ | Component in the axial direction, |
| $\theta$ | Component in the tangential direction, |

**Superscripts**

| | |
|---|---|
| $in$ | Inlet condition, |
| $OD$ | On-design condition, |
| $OFF$ | Off-design condition |
| $out$ | Outlet condition, |

predecessor, diabatic – DCAES–, is the lack of external energy sources supplying heat prior to the expansion stages. In DCAES, a combustion chamber is responsible for re-heating the air, whilst in ACAES, the heat of compression is stored and recycled [10].

This heat recycling is the key feature that enables ACAES to be a potentially excellent net-zero storage technology. However, it also imposes a major challenge to the system operation, design and performance. Since there is no external heat supply, the expander inlet temperature is limited by, and heavily coupled to, the compressor outlet temperature [11]. Moreover, the heat exchangers and TES will always introduce some temperature drop, which further aggravates this limitation. Whilst conventional gas turbines, and the turbines in DCAES systems, tend to operate at high temperatures (over 800 K in McIntosh [12], 760 K in Huntorf [13] and over 2000 K in modern gas turbines for power generation [14]), in ACAES the expanders must operate at temperatures akin to sub- and supercritical steam turbines, 500 [15]–800 [16] K

The strong coupling between the charging and discharging processes in ACAES leads to challenges and unconventional operation requirements in the compressors, heat exchangers, TES and turbines. Conserving the heat at high temperatures – and, therefore, reversibility – becomes paramount in achieving acceptable performance. DCAES, on the other hand, does not experience this coupling. In the McIntosh plant, the compressor train maximum outlet temperature is around 450 K with unbalanced intercooler operation, cooling the air down without conserving high temperature in the coolant, which only reaches ≈305 K [17]. Similarly, the three intercoolers and single aftercooler in the Huntorf compressor train cool the air from between 417 and 508 K down to 315 K [13]. In TICC-500, a rare example of a well-documented ACAES full-plant experimental study, compression heat losses and inefficiencies in the TES system directly contributed to the lower-than-anticipated system performance, with an experimental round-trip efficiency (RTE) of 23.7% instead of the predicted 40.7% [18].

Therefore, the authors postulate that, *for satisfactory ACAES performance,* ***compressors*** *must be able to efficiently operate with higher outlet temperatures,* ***heat exchangers*** *must be highly effective and reversible and* ***turbines*** *must operate with lower inlet temperatures without compromising efficiency*. The requirement for this level of redesign across multiple components is a primary reason that, despite significant funding, a viable ACAES design does not yet exist. Beginning to address this crucial knowledge gap, this paper aims to deal with the compressor design. By designing an application-specific axial-flow compressor, it is expected that the machine operates efficiently in on- and off-design conditions with minimal inter- and after-cooling. The importance of utilising detailed compressor design and performance prediction in ACAES has been discussed in [19]. In the literature, there are some publications that do consider an off-design performance penalty, such as [20–22]. However, these use generic mathematical models, based on semi-empirical correlations developed for conventional centrifugal compressors, without any remarks to technology type, compressor geometry or performance calculation. Polynomial interpolation has also been implemented to introduce an off-design penalty, e.g. [23,24].

While indicative, this previous work neglects practical limitations that arise from designing a compressor for ACAES. Ultimately, this arises from the fact compressor operation is highly specific to the actual compressor geometry, and generalised performance maps cannot be reliably assumed from compressors in other applications. To the best of our knowledge, this paper presents the first detailed compressor design and the associated performance map for a specifically-designed ACAES compressor.The designed compressor is able to output air at the required pressure range, between 5.5 and 7.7 MPa, at a power consumption of 43 to 62 MW, and operating with variable angular speed and adjustable Inlet Guide Vanes. The designed compressor is split into two spools, which rotate at different, but proportional, speeds, consisting of 33 stages divided as 18 in the first spool and 15 on the second. The authors opted to develop an axial compressor, which requires more stages than centrifugal machines to achieve the same outlet pressure. This in turn means that the off-design penalty is spread, decreasing the stage-specific performance degradation, at the expense of narrowing the stable operation range due to incidence angle departure ($\imath^{OFF} - \imath^{ON}$) building up from inlet to outlet. In off-design conditions, the flow turning imposed by each blade row is different from the design value, which leads to the downstream blade rows to receive the air at an incidence angle increasingly farther from the design, which can lead to a potentially excessive incidence angle deviation, increasing losses and inducing instabilities, particularly on rear-stages [25,26] (see Section 3.2.2). The compressor design and performance prediction procedure follows the Reference Radius Method (RRM) to generate the preliminary design, followed by the inviscid Throughflow Method (TFM) to define a reliable geometry and establish the on- and off-design performance. It is expected that the designed compressor is able to operate at a high isentropic efficiency within the relevant pressure range, whilst preserving the airflow high temperature and allowing the system to operate at a round-trip efficiency similar to the systems reported in literature, *e.g.,* 70% in [22,27], up to 75% in [24] and 64% in [28].

## 2. Adiabatic Compressed Air Energy Storage: thermodynamic model and compressor requirements

Fig. 1 depicts the proposed ACAES system. Each compressor spool consists of an IGV row, whose function is to initiate the flow conditions by providing the appropriate incidence angle upon the first rotor row, followed by $S$ stages (rotor + stator), and the OGV, responsible for removing the tangential velocity component from the airflow. During system charging, once the airflow has left a compressor spool, it is decelerated in an ideal diffuser, recovering the dynamic pressure and temperature. The airflow is then cooled to near-ambient temperature in a heat exchanger and it is either delivered to the second spool (intercooler – IC) or into the underground storage (aftercooler – AC). Each charging heat exchanger is assumed to be capable of outputting air at a fixed temperature (313.15 K), by varying the coolant flow such that the heat capacity ratio $C_r$ is kept at 0.9, with $C_{air} < C_{cool}$. The instantaneous effectiveness $\varepsilon$ is calculated and stored as a function of the coolant outlet temperature ($\varepsilon = f(T^{out}_{cool})$) [29]. Each heat exchanger imposes a 5% pressure drop [13].

The 300,000 m$^3$ high pressure air store cycles between a minimum of 5.5 MPa and a maximum of 7.7 MPa. It operates adiabatically during the system charging and discharging, whilst allowing the stored air to return to ambient temperature in between [6,29]. The storage maximum and minimum pressures have been chosen to be similar to the two commercially available plants in operation, Huntorf 4.6–7.2 MPa and

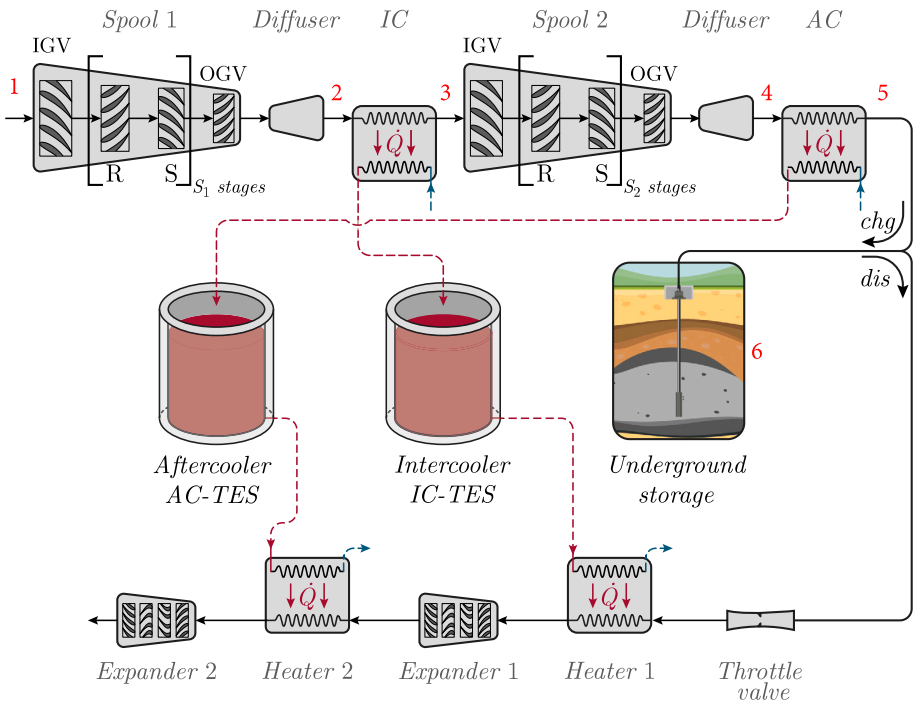


**Fig. 1.** Proposed ACAES system: two spool compressor, each with inlet and outlet guide vanes, followed by a diffuser and a inter/after cooler. Two insulated sensible heat TES tanks mix and store the thermal fluid incoming from the charging heat exchangers. The underground storage is a 300,000 $m^3$ cavern, cycling between 5.5 and 7.7 MPa. The discharging section consists of a throttle valve and two expanders preceded by a heater heat exchanger.

McIntosh 4.6–7.5 MPa [10]. The coolant outflowing from the charging heat exchangers enters the TES tanks, wherein it is irreversibly and uniformly mixed with any previously stored coolant. During discharge, air is released from the high pressure store, via the throttle valve, which is set to 5.5 MPa, again similar to Huntorf and McIntosh [10]. The discharging heaters construction is similar to the IC/AC, and thus, effectiveness is taken from the values recorded during discharge at the corresponding TES temperature (see Section 2.2), whilst also imposing the same pressure drop of 5%.

### 2.1. System and components models

The ACAES model is developed using the finite time-step approach, in which a *quasi-steady* state analysis calculates the thermodynamic state evolution at the inlet and outlet of each component, coupling adjacent components (no loss between components is considered). Within each time-step, $\Delta t = t_2 - t_1$, all properties and functions are evaluated at the initial instant $t_1$ such that $\int_{t_1}^{t_2} f(t)dt \approx f(t_1)\Delta t$ and $f(t_2) = f(t_1) + \frac{\Delta f(t)}{\Delta t}\Delta t$. All thermodynamic properties were obtained from the CoolProp package for Matlab [30].

The system operation is divided into four subsequent stages: (i) *charging*: during which the compressors draw power from the grid and compress the air, converting the electricity into thermal and potential mechanical energy; (ii) *idle*: a stand-by phase during which no air is moved; (iii) *discharging*: air is released from storage and is expanded in turbines which power electrical generators, returning the energy to the grid; (iv) *recovery*: an interim between the end of discharging and the beginning of the next changing cycle.During the idle and recovery periods, the compressed air stored in the high-pressure store is considered to return to the underground temperature, which in turn, is assumed equal to ambient. Furthermore, as reported in [31], it can be noted that the ambient temperature assumed is not far from the conditions in Huntorf, where the cavern temperature typically varies between 30 and 10 °C. The system round-trip efficiency $\eta_{RTE}$ is calculated by the ratio between the energy generation (during discharging, Eq. (15)) and consumption (during charging, from performance map):

$$\eta_{RTE} = \frac{\int_0^{t_{dis}} \dot{W}_{dis} dt}{\int_0^{t_{chg}} \dot{W}_{chg} dt} \approx \frac{\sum_0^{t_{dis}} \dot{W}_{dis} \Delta t}{\sum_0^{t_{chg}} \dot{W}_{chg} \Delta t} \tag{1}$$

As previously explored in [6], the variable storage pressure inherent to isochoric CAES systems leads to an imbalance between the added and extracted air masses in the first few full charge–discharge cycles. After a few cycles (approximately 5), the operation is sufficiently stabilised and the performance settles at it nominal value. Therefore, the system simulation will take this effect into account, running successive charging-idle-discharging-recovery (Solution Run - $SR$) until a stable operation is achieved. Moreover, the ACAES components modelling has been developed using the conventional black-box models, wherein a set of input conditions determine the component performance and output properties, without reference to the detailed internal construction of components. This classical thermodynamic approach has a key benefit of simplifying the analysis, whilst also providing a clear set of design objectives, *i.e.,* establishing the correlations between inputs and desired outputs, which can be used as guidelines in designing the components. In the case of the present study, the compressor guidelines stemming from the *black-box* approach indicate that it is advantageous to conserve high airflow temperatures, whilst the compressor runs with elevated isentropic efficiencies and mass flow rates within the required operating range [11].

### 2.2. Heat exchangers

The heat exchangers are responsible for removing the thermal exergy from the airflow after the compressors (inter- and aftercoolers in charging) or reintroducing it to the airflow in the reheaters during discharging. Although the mathematical model applied to IC, AC and heaters is similar, there are operational differences between charging and discharging. During the system charging, it is assumed that the inter- and after-cooler are able to cool the airflow down to a fixed outlet temperature, 313.15 K, regardless of the inlet air temperature

and heat capacity. To achieve this, the coolant mass flow rate and heat exchanger effectiveness are variable, whilst the heat capacity ratio $C_r$ is kept at 0.9, with the air heat capacity always smaller than the coolant to ensure it undergoes the greatest temperature variation. In these cases, the coolant enters the inter- and after-coolers at ambient temperature. No particular heat exchanger geometry is assumed, and a 5% pressure drop is assumed, similar to the figures reported in [13,23].

$$\begin{aligned} &Q_{air} = Q_{cool} = Q_{IC,AC} = \varepsilon C \Delta T, \\ &T_{air}^{out} = 313.15 \text{ K}, \\ &T_{cool}^{in} = 298.15 \text{ K}, \\ &C = \dot{m} c, \\ &C_r = \frac{C_{min}}{C_{max}} = \frac{C_{air}}{C_{cool}} = 0.9 \end{aligned} \tag{2}$$

Conversely, during the system discharge the air mass flow rate and thermal fluid inlet temperature are constant while the air inlet temperature decreases slightly as the HPST cools (see Fig. 8). In such conditions, the discharge heat exchangers operate with constant effectiveness and variable outlet temperature. Moreover, the effectiveness value used is taken from data recorded during the system charging, by taking the effectiveness as a function of the hot fluid temperature (air during charging, coolant during discharging). Once the coolant leaves the heat exchanger it is stored in a cold tank and assumed to reach ambient temperature by the next cycle. All heat exchangers operate with Dowtherm A as coolant, and according to the manufacturer data sheet [32], the thermal fluid (coolant) specific heat – $c_{cool}$ – at various temperatures can be modelled as

$$c_{cool}(T) = 2.915\ T\ [\text{K}] + 708.4 \tag{3}$$

where $c_{cool}$ is given in J kg$^{-1}$ K$^{-1}$, the temperature $T$ must be in kelvin. This correlation is valid for $288 \leqslant T \leqslant 678$ K.

### 2.3. TES

The Thermal Energy Storage (TES) units store thermal exergy removed from air post-compression, and later deliver it to be recombined prior to expansion. Ideally, the TES unit would operate without exergy destruction due to mixing heat at different temperatures, *i.e.*, perfect thermal-stratification. However, in fluids internal heat diffusion tends to homogenise temperature over the storage period. Therefore, the TES units are always considered to be uniformly mixed. The thermal fluid coming from the charging heat exchangers – inter- and after-cooler – is stored until it is supplied to the heaters during discharging. The mass and energy balance applied to the thermal energy store during charging yields

$$m_{cool,2}^{TES} = m_{cool,1}^{TES} + \dot{m}_{cool} \Delta t, \tag{4}$$

$$m_{cool,2}^{TES} c_{cool,2}^{TES} T_{cool,2}^{TES} = m_{cool,1}^{TES} c_{cool,1}^{TES} T_{cool,1}^{TES} + \dot{m}_{cool} c_{cool} T_{cool} \Delta t, \tag{5}$$

where $m_{cool,j}^{TES}$ is the coolant mass stored (kg) in each TES tank at instant $j$, wherein $j = 1$ stands for the timestep beginning and $j = 2$ corresponds to the end. $\Delta t$ is the timestep increment, in seconds, $c_{cool}$ is the temperature-dependent coolant specific heat capacity (J kg$^{-1}$ K$^{-1}$, see Eq. (3)), $T_{cool}$ is the coolant temperature in K and $\dot{m}_{cool}$ is the coolant mass flow rate from the correspondent charging heat exchanger, in kg s$^{-1}$. During the idle period, no mass or heat loss is assumed in the TES. During discharging, the TES temperature remains constant, therefore only the mass balance (Eq. (4)) is used, with a negative mass flow rate indicating the coolant outflow.

It can be noted that the presented TES model is not likely to be well-suited for grid-scale ACAES systems, since the mass of coolant required will scale rapidly. However, a more intricate model is not considered, since the main research goal is to address the effects and impacts of the compressor operation in the system. Further research can and should utilise the compressor results presented here and expand them to accommodate a detailed heat exchanger and TES analysis.

### 2.4. Throttle valve

The throttle valve is assumed adiabatic isenthalpic. Under ideal gas assumptions, wherein $h = f(t)$, the throttle valve should also be isothermal but, by taking the actual fluid properties from CoolProp, a temperature drop is observed. The magnitude of this effect decreases as the discharging process takes place and the throttle ratio $(P^{HPST}(t)/P^{thr})$ approaches unity.

$$h^{out}(t) = h(h = h^{HPST}(t)) \tag{6}$$

$$T^{out} = T(h = h^{out}, P = P^{thr}), \tag{7}$$

### 2.5. High pressure air store (HPST)

The High-pressure store (HPST) is responsible for receiving and keeping the compressed air until a net energy demand requires the ACAES facility to discharge. Effectively, the HPST stores energy as non-flow physical exergy due to pressure. When the ACAES system is under charging, the mass increment to the store increases the storage pressure, compressing the previously stored air to a new equilibrium pressure. Conversely, when the system is discharging, the outflowing mass decreases the store pressure and temperature. This process can be modelled under uniform transient analysis applying mass and energy conservation

$$m_2(t) = m_1(t) \pm \dot{m}(t) \Delta t, \tag{8}$$

$$u_2(t) = \frac{m_1(t) u_1(t) \pm \dot{m}(t) h(t) \Delta t}{m_2(t)}, \tag{9}$$

$$T_2(t) = T(u = u_2(t)), \tag{10}$$

$$P_2(t) = P(T = T_2(t), v = V_{HPST}/m_2(t)) \tag{11}$$

where $m_1$ and $m_2$ are the timestep initial and final stored air mass, $\dot{m}$ is the mass flow rate flowing into (charging, + ve sign) or out of (discharging, −ve sign) the HPST, $u_1$ and $u_2$ are the stored air initial and final specific internal energy, $h$ is the specific enthalpy, whose value is either the final aftercooler air outlet enthalpy (charging) or the store timestep initial specific enthalpy (discharging). Once the updated internal energy, $u_2$ has been calculated, it is used in conjunction with the updated specific volume, $v_2$, to determine the updated temperature and pressure.

Once charging or discharging processes are completed, the HPST enters the idle and recovery periods, respectively. These are characterised by no mass flow into or out of the storage, and it is assumed that during such periods, there is enough time to allow the stored air temperature to equalise with ambient (see Fig. 8). The final pressure after such periods can be calculated as an isochoric transformation

$$P^{idle,rec} = \frac{T_a}{T^{fin}} P^{fin} \tag{12}$$

where $P^{idle,rec}$ is the equilibrium idle or recovery pressure, $T_a$ is the ambient temperature and $P^{fin}, T^{fin}$ are the final charging or discharging pressure and temperature, respectively. Finally, the idle and recovery heat exchange is calculated as the difference between the equilibrium idle/recovery and the final charging/discharging internal energies.

$$Q^{idle,rec} = m \left( u^{idle,rec} - u^{fin} \right) \tag{13}$$

### 2.6. Expanders

Given the presence of an upstream throttle valve (see Fig. 1), the expander operates with constant mass flow rate, under fixed inlet pressure and expansion ratio. The expander analysis does not take into account any dynamic effects, instead only takes the inlet and outlet thermodynamic properties. The instantaneous expander power output $\dot{W}_e(t)$ is calculated as

$$\dot{W}_e(t) = \eta_s \dot{m}^{dis} \left( h_{in}(t) - h_{out,s}(t) \right) \tag{14}$$

**Table 1**
Qualitative comparison between conventional components capabilities and the unusual ACAES requirements [11].

| | Conventional capabilities | ACAES requirements |
|---|---|---|
| Compressors | • **Minimise** power input<br>• **Lower** outlet temperature<br>• **High** isentropic efficiency | • **Maximise** outlet temperature<br>• **Lower** number of intercoolers<br>• **High** isentropic efficiency |
| Heat exchangers | • **Maximise** effectiveness<br>• **Minimise** pressure drop<br>• **High** heat capacity imbalance | • **Minimise** power input<br>• **Lower** outlet temperature<br>• **High** isentropic efficiency |
| Expanders | • **Maximise** power output<br>• **Maximise** inlet temperature<br>• **High** pressure ratio<br>• **High** isentropic efficiency | • **Maximise** power output<br>• **Lower** inlet temperature<br>• **Lower** pressure ratio<br>• **High** isentropic efficiency |
| Optimisation | • Individual components | • System as a whole |

where $\eta_s$ is the expander isentropic efficiency, $m^{dis}$ is the discharging mass flow rate (90 kg $s^{-1}$, see Table 5), $h_{in}$ and $h_{out,s}$ are the inlet and isentropic outlet specific static enthalpies. The output energy ($W_e$) over a $\Delta t$ time interval is simply

$$W_e(\Delta t) = \int_{t_1}^{t_2} \dot{W}_e(t)dt \approx \dot{W}_e(t_1)\Delta t \tag{15}$$

### 2.7. Components: ACAES requirements vs. off-the-shelf capabilities

Conventional compressors, and the compressors used in DCAES plants, tend to stack intercoolers to lower subsequent stages inlet temperature, which decreases the specific work input and capital costs. This is allowable when an external heat source is used to provide high enthalpy air (through combustion) at the expander inlets, as is the case in the Huntorf and McIntosh plants [12,13]. The compressor intercoolers are then highly imbalanced which leads to high effectiveness. This not possible in ACAES since the expander inlet temperature can only be as high as the coolant from the intercooler. Hence from a theoretical perspective, the optimal condition – in terms of heat capacity – would be a balanced heat exchanger. However, in practice this corresponds to a minimum effectiveness [33].

Conventional compressors and gas intercoolers are, therefore, not suitable for ACAES. Further evidencing the lack of market ready compressors capable of operating within ACAES requirements, a recent CAES white paper published by Siemens Energy [34] makes no remark to adiabatic systems, but instead, only considers fired systems. Hence the compression train should be redesigned to abide by ACAES requirements, as summarised in Table 1. The design and performance analysis procedures will be conducted in accordance with the well-established and validated reference radius and throughflow methods. The principal design objective is to create a plausible compressor geometry and its associated operation map within the defined operational range.

So far, there are four ways in which the compressor operation is treated in papers describing ACAES models: *(i)* A fixed mass flow rate and efficiency are assumed (vast majority of publications) and the compressor power consumption increases with air storage pressure. *(ii)* Simple numerical correlations are used (*i.e.* [23,33]), which seek to artificially introduce an off-design performance penalty based on the general shape of turbomachinery performance curves. *(iii)* Experimental analysis which measures the actual performance of a compressor connected to a pressure vessel under variable load conditions. In [35], a 5.2 MW centrifugal compressor, proposed for ACAES applications, is tested in off-design conditions. However, the is only able to reach a stagnation pressure ratio of ≈2.4, meaning more stages would be necessary to reach conventional CAES pressures. The interaction between stages aiming a system-level optimisation was not analysed. *(iv)* Generalised performance prediction methods are used, such as Flugel formulas (*i.e.* [22,36–39]), which establish correlations between prescribed design performance values and typical off-design relative behaviour, without a corresponding compressor geometry. The shortage of publications that associate a compressor performance to an actual design exposes a key knowledge gap that this paper aims to fulfil, bridging the conventional *black-box* approach to a robust and well-established compressor design procedure. Notably, the mean-line approach developed in [19] stands out, where a preliminary centrifugal compressor geometry, associated with semi-empirical loss correlations, is optimised to maximise single-stage efficiency and minimise the required number of stages.

## 3. Axial-flow compressor design and performance

The axial flow compressor will be designed using two methodologies: (*i*) the reference radius (or mean-line) method, in which the preliminary geometry (*i.e.*, flowtrack dimensions and number of stages) is defined, followed by an initial flow stability check for a set of dimensionless design coefficients and the on-design operational values for mass flow rate and rotational speed. Following, (*ii*) the Throughflow (or streamline curvature) Method takes the preliminary results from (*i*) as inputs to define the final geometry and predict the performance in on- and off-design conditions [25,26,40,41]. The design methodologies applied are well-established, extensively employed, and time tested. This ensures that the resulting geometry and performance map can be confidently regarded as a fitting approximation of reality. The novelty, therefore, lies in its application to ACAES, incorporating the system's operational requirements and resulting in a performance map attached to a preliminary geometry.

The global design procedure can be split into two key processes: the *design process* itself, wherein the compressor geometry is generated and its performance is predicted, followed by the *solution quality assessment*, which takes the *design process* output and, qualitatively and quantitatively, checks for the flow stability (Section 3.2.3) and performance. In case a solution fails the *solution quality assessment* during the RRM and on-design TFM phases, the design parameters and variables are updated and the whole *design process* restarts. This update is manually implemented by changing the dimensionless design coefficients, within ranges defined in literature, and analysing the impacts on the output geometry and performance. The numeric changes themselves involved an analysis of their definitions and a systematic trial-and-error approach. During the off-design TFM procedure, various operating conditions are tested for flow stability and performance, generating a compressor map.

### 3.1. Reference Radius Method - RRM

The RRM simplifies the flow across the entire annulus section to a single location, referred to as the *reference radius*, $r_{ref}$. This way, by solving the velocity field and compressible aero-thermodynamic equations on $r_{ref}$ for all stations,[1] the airflow properties are defined and assumed valid for the entire radial cross section [25,26]. The RRM defines the hub, reference and tip radii for all $S$ stations, i.e., from the IGV inlet ($i = 0$) up to the OGV outlet ($i = S$). In axial-flow machines, the reference (or mean) radius is defined as the locus that equally divides the annulus cross section area, calculated as root-mean-square between the blade hub and tip radii, depicted in Fig. 2(a) and defined by Eq. (16).

$$r_{ref} = \sqrt{\frac{r_{hub}^2 + r_{tip}^2}{2}}, \tag{16}$$

In addition to the reference radius being considered as representative of the entire flow along a specified radial station, the RRM also makes the following additional assumptions:

[1] Defined as the bladeless section between adjacent blade rows, as well as before the Inlet Guide Vane (IGV) inlet and after the Outlet Guide Vane (OGV) outlet.

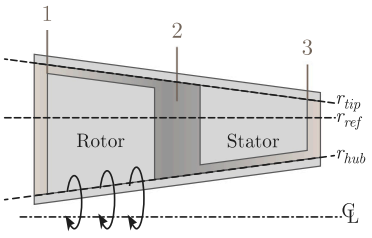


(a) Hub, reference and tip radii in a repeating stage (R+S). Station 1 corresponds to the rotor inlet, 2 to the rotor outlet and stator inlet and 3 is the stator outlet.

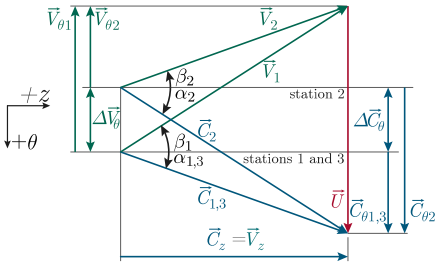


(b) Typical RRM velocity diagram for a repeating stage axial flow compressor.

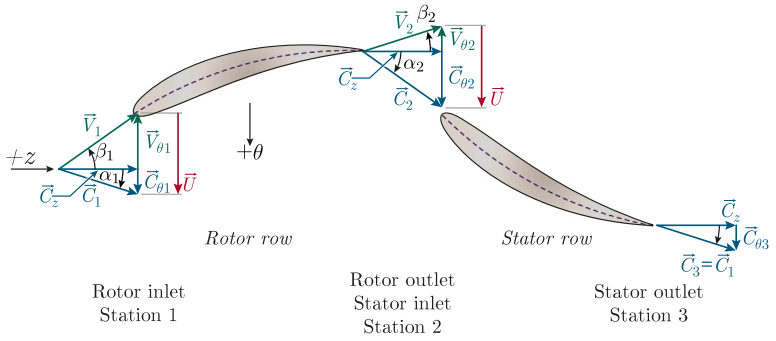


(c) Flow angles and velocities across an axial-compressor stage under repeating stage RRM analysis.

**Fig. 2.** Axial-flow compressor: (a) repeating stage schematic representation; (b) typical velocity diagram under repeating stage assumptions and; (c) flow and angles within a stage.

(A.1) Air is treated as an ideal gas;
(A.2) Flow is adiabatic;
(A.3) Constant axial velocity component;
(A.4) Radial velocity and momentum neglected;
(A.5) Reference radius constant;
(A.6) Repeating stage;
(A.7) Inviscid flow;

Assumptions (A.1) and (A.2) are common in flow-machinery contexts [25,26,41–43], whilst (A.3) and (A.4) ensure that the RRM remains simple enough to be used as a quick preliminary design method with reasonable compromise to accuracy [25]. The repeating stage (A.6) is a simplification that stems from the constant reference radius (A.5) and axial velocity (A.3), which allows for a single velocity diagram (Fig. 2(b)) to correspond to all stages within the spool, in spite of the variable geometry [26]. A further consequence of the repeating stage assumption is that the absolute velocities and flow angles on the rotor inlet (station 1) are the same as on the stator outlet (station 3). Assumption (A.7) eliminates higher order viscous dissipation terms in the flow equations, ensuring that the flow field equations are numerically stable and easily solvable. The viscous dissipation and boundary layer effects are artificially introduced as semi-empirical loss coefficients [26].

The velocity diagram for a typical axial-flow compressor stage is depicted in Fig. 2(b). Fig. 2(b) also shows that the axial velocity components are independent of the chosen frame of reference ($\vec{C}_z = \vec{V}_z$). The Euler Equation for Turbomachinery [43] (Eq. (17)) correlates the change in tangential velocity to the stage specific work $\Delta w$, in J kg$^{-1}$,

$$\Delta w = \omega r_{ref} \Delta C_\theta = \omega r_{ref} \Delta V_\theta, \tag{17}$$

where $r_{ref}$ is given in m and the change in tangential velocity, $\Delta V_\theta = \Delta C_\theta$ is expressed in m s$^{-1}$.

The first step in the RRM process consists of defining the design mass flow rate $\dot{m}^{OD}$, rotational speed $\omega^{OD}$ and limiting outlet conditions (*e.g.*, design outlet pressure or maximum temperature allowable in downstream component). For any annulus bladeless section, the mass flow rate can be calculated by Eq. (18)

$$\dot{m} = \rho C_z A = \rho C_z \pi \left( r_{tip}^2 - r_{hub}^2 \right), \tag{18}$$

where $\rho$ is the static density, in kg m$^{-3}$, $C_z$ is the axial velocity component, m s$^{-1}$, and $A$ is the annulus cross section are, in m$^2$. Therefore, for a given design mass flow rate and known static density, choosing an axial velocity components sets the annular cross sectional flow area. Then, by choosing the $r_{ref}$, the hub and tip radii on each station are defined. The manipulation of $C_z$ allows for controlling the blade height ($\mathbb{H} = r_{tip} - r_{hub}$), for a fixed area, on a blade row. On a given radial station $i$, the static density calculation (Eq. (18)) depends on the upstream station ($i-1$) aero-thermodynamic properties being known.[2] Then, the effects of the blade row between stations $i-1 \rightarrow i$ on the airflow are accounted for, and the outlet velocities and static pressure and temperature are calculated. Once static and dynamic properties on station $i$ are fully determined, it becomes the known inlet reference for the downstream station $i+1$. This solution marches along all stations ($i = [0..\mathcal{S}]$, where $\mathcal{S}$ is the OGV outlet station) on an axial-flow compressor. The detailed blade row calculating procedure is presented in Sec. SM.1

The flow coefficient $\varphi$ corresponds to the ratio between axial and blade tangential velocities, allowing for inlet and outlet angles to be correlated as shown in Eq. (19).

$$\begin{aligned} \varphi &= \frac{C_z}{U}, \\ \frac{1}{\varphi} &= \tan\alpha_1 + \tan\beta_1 = \tan\alpha_2 + \tan\beta_2 \end{aligned} \tag{19}$$

The load coefficient $\psi$ (defined in Eq. (20)) correlates how much energy is absorbed by the fluid (as stagnation enthalpy rise). Ideally, higher values of load coefficients would be desirable, as they correspond to a greater stage specific pressure increase and blades being more efficiently loaded [25,26]. However, as the stagnation enthalpy

[2] In case of IGV inlet, $i = 0$, it is assumed that ambient conditions correspond to inlet stagnation properties ($T_\emptyset^{i=0} = T_a$, $P_\emptyset^{i=0} = P_a$) and the airflow velocity is entirely axial ($C = C_z$) [25,26,29].

**Table 2**
Recommended values for the main dimensionless design parameters used in the Reference Radius Method.

| Variable | Symbol | Recommended | Ref. |
|---|---|---|---|
| Flow coefficient | $\varphi$ | 0.4–0.8 | [25] |
| Load coefficient | $\psi$ | <0.6 | [25] |
| Degree of reaction | $\mathcal{R}$ | 0–1 | [25] |
| Blade aspect ratio | $\Lambda$ | 0.8–1.5 | [40,45] |
| Solidity | $\sigma(r_{ref})$ | 0.8–1.5 | [25,26] |

rise is achieved by decreasing the local flow velocity, an excessive loading results in boundary layer detachment and flow reversal. Therefore, in practical scenarios, the load coefficient is limited to 0.6 (highly loaded, diffusion controlled blades [25]), and most designs have $\psi \leq 0.4$ to ensure sufficient stall safety margin [26,44].

$$\begin{aligned} \psi &= \frac{\Delta h_{\emptyset}}{U^2} = \frac{\Delta C_{\theta}}{U}, \\ \psi &= 1 - \varphi\left(\tan\alpha_1 + \tan\beta_2\right), \end{aligned} \tag{20}$$

The degree of reaction ($\mathcal{R}$, Eq. (21)) corresponds to the ratio between the static enthalpy rise in the rotor over the rise across the total stage (R + S). It compares how the stage specific compression work load is divided between the rotor and stator.

$$\begin{aligned} \mathcal{R} &= \frac{h_2 - h_1}{h_3 - h_1}, \\ \mathcal{R} &= 1 - \frac{C_{\theta,1} + C_{\theta,2}}{2U} \end{aligned} \tag{21}$$

Finally, rearranging Eqs. (19)–(21) allows the determination of the inlet and outlet flow angles across any blade row on the reference radius locus as presented in Eq. (22).

$$\begin{aligned} \tan\alpha_1 &= \frac{1 - \mathcal{R} - \psi/2}{\varphi}, & \tan\beta_1 &= -\frac{\mathcal{R} + \psi/2}{\varphi}, \\ \tan\alpha_2 &= \frac{1 - \mathcal{R} + \psi/2}{\varphi} & \tan\beta_2 &= -\frac{\psi/2 - \mathcal{R}}{\varphi}, \end{aligned} \tag{22}$$

A purely geometric dimensionless design parameter is the blade aspect ratio, $\Lambda$, defined as the ratio between the blade height $\mathbb{H}$ over the chord length $\mathbb{C}$. The final dimensionless design parameter presented here is the blade solidity ($\sigma(r)$). It is defined in Eq. (23) as the ratio between the blade chord ($\mathbb{C}$) and the local pitch distance ($\mathbb{S}(r)$) between adjacent blades along a given radial position, and measures the relative blade spacing on a blade row. Unlike the previous dimensionless design parameters, the solidity is not constant across a stage, as it depends on the radial position. The solidity is a key factor in determining the losses across a blade row, and values close to unity generally represent a near-optimum condition[3] [29,40,41]. For constant chord length blades, the solidity decreases from hub to tip due to pitch increase.

$$\sigma(r) = \frac{\mathbb{C}}{\mathbb{S}(r)}, \tag{23}$$

Table 2 presents a brief guideline of values recommended in the literature for the aforementioned design parameters. Note that the solidity values are evaluated on the reference radius.

An indicative step-by-step RRM application guide can be found in the Supplementary Material, Sec. SM.1.

### 3.1.1. Losses

The loss calculation procedure begins with the definition of which blade profile is used. Conventional options, such as the American NACA 65XX or British DCA C.4 series have been extensively tested and are widely reported on literature, and therefore, numerous semi-empirical correlations are available [26,46–49]. Novel alternatives, such as tandem blades [50–52], have been proposed in literature with promising results. However, due to their novelty, there are significantly fewer loss coefficients correlations proposed so far. Hence, in this paper, the NACA 6510 blade series is used [53].

The notation presented in this section covers the rotating set of blades. To apply it to stationary blade rows, $(\vec{V}, \beta)_{1,2,m} \rightarrow (\vec{C}, \alpha)_{2,3,m}$. Furthermore, the stagnation pressure loss mechanism is a complex, multi-factor coupled phenomena which includes profile drag, boundary layer detachment, secondary flow structures, wake mixing, edge vortices, end-wall blockade and tip scrubbing [29]. Each of these interact with the others, resulting in an intricate, inherently transient and non-uniform loss mechanism. To simplify the calculation procedure, 2D cascade experimental data were used to develop equations that predict each loss component independently. Their combined effect is assumed to be the sum of the individual pressure losses:

$$\zeta_P = \sum \zeta_{p,i} \tag{24}$$

Two dimensionless operation parameters useful to calculate the flow stability and the magnitude of the loss components are the Diffusion Factor, $DF$ and Liblein's Equivalent Diffusion Factor $DF_{EQ}$, calculated by Eqs. (25) and (26) [26]

$$DF = 1 - \frac{V_2}{V_1} + \frac{V_{\theta,1} - V_{\theta,2}}{2\sigma V_1}, \tag{25}$$

$$DF_{EQ} = \frac{V_{max}}{V_1}\frac{V_1}{V_2} \tag{26}$$

where $V_{max}$ is the maximum airflow velocity between the inlet and outlet sections (along the blade row). In [54], Lieblein developed a correlation to be used on-design condition (Eq. (27)), later modified to also be used off-design [55], presented in Eq. (28)

$$\left(\frac{V_{max}}{V_1}\right)^{OD} = 1.12 + 0.61\frac{\cos^2\beta_1}{\sigma}\left(\frac{r_1 C_{\theta,1} - r_2 C_{\theta,2}}{r_1 C_z}\right), \tag{27}$$

$$\left(\frac{V_{max}}{V_1}\right)^{OFF} = \left(\frac{V_{max}}{V_1}\right)^{OD} + 0.0117\,|\delta\imath|^{1.43} \tag{28}$$

In Eq. (27), $r_1 = r_2 = r_{ref}$ for repeating stages (A.6), while in Eq. (28), $\delta\imath$ is the incidence angle departure, calculated as $\delta\imath = \imath^{OFF} - \imath^{OD}$ and used for off-design analysis (see Section 3.2.2). We consider three loss mechanisms: (1) Primary loss, (2) Secondary flow losses, and (3) End-wall losses. The primary loss (1) consists of the profile drag and wake mixing losses. The secondary flow (2) loss coefficient, $\zeta_2$ encompasses the stagnation pressure drop due to flow structures not displayed on the velocity diagram, Fig. 2(b). These include vortex formation between blades, separation zones and unwanted re-circulation . Finally, the end-wall loss (3) coefficient, $\zeta_{ew}$ covers the loss induced by the interaction between the main airflow and the low-energy flow in the boundary layers on the hub and shroud surfaces. The loss coefficients, $\zeta_1$ through $\zeta_{ew}$, can be calculated according to Eqs. (29) through (31) [26,49,54,56]

$$\text{Primary}\begin{cases} \zeta_1 = 8\cdot 10^{-3}\left[\dfrac{\sigma}{\cos\beta_2}\left(\dfrac{V_2}{V_1}\right)^2\right]\left(1 + 3.1\left(DF_{EQ} - 1\right)^2 \right. \\ \qquad \left. +0.4\left(DF_{EQ} - 1\right)^8\right) \end{cases} \tag{29}$$

$$\text{Secondary}\begin{cases} C_{D,s} = 0.018 C_L^2, \\ \beta_m = \arctan\left[0.5\left(\tan\beta_1 + \tan\beta_2\right)\right], \\ \zeta_2 = C_{D,s}\sigma\dfrac{\cos^2\beta_1}{\cos^3\beta_m}, \end{cases} \tag{30}$$

$$\text{End-wall}\begin{cases} C_{D,ew} = 0.02\dfrac{1}{\sigma\Lambda}, \\ \zeta_{ew} = C_{D,s}\sigma\dfrac{\cos^2\beta_1}{\cos^3\beta_m}, \end{cases} \tag{31}$$

[3] In terms of minimising the losses across a blade row.

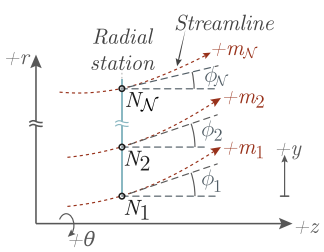


(a) Radial station (*quasi-normal*) discretisation, depicting nodes $N_1$ through $N_{\mathcal{N}}$, each with a streamline angle $\phi$ encompassed between the streamwise direction $+m$ and the axial direction, $+z$. The *quasi-normal* direction $+y$ is depicted, such that when $r = r_{hub} \rightarrow y = 0$.

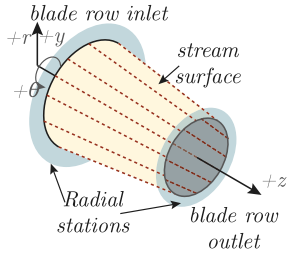


(b) One stream surface generated by revolving streamlines (brown) around the axial direction $+z$ between radial stations located at a blade row inlet and outlet.

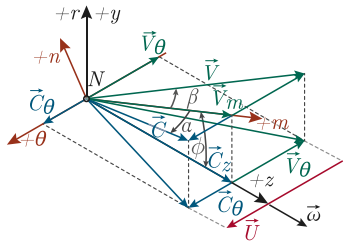


(c) Typical TFM velocity diagram depicting the absolute and relative velocities and flow angles calculated on a node. In brown, the three mutually orthogonal natural coordinates ($+m \perp +n \perp +\theta$). Note that $\vec{C}_m = \vec{V}_m$ and $\vec{C}_z = \vec{V}_z$.

**Fig. 3.** Key concepts and schematic depiction of the TFM. (a) Radial (*quasi-normal*) stations discretisation with nodes located along streamlines; (b) stream surface generated from revolving streamlines around axial direction $+z$, and; (c) velocities and flow angles on the nodes.

where $C_L$ is the lift coefficient, $\beta_m$ is the mean flow angle, $C_{D,s}$ is Howell's secondary flow drag coefficient and $C_{D,ew}$ is the end-wall drag coefficient

### 3.2. Throughflow Method - TFM

Once the RRM has been run, the required number of stages, preliminary flowtrack geometry and axial length are defined. However, the RRM overlooks all flow effects which do not occur specifically at the reference radius. Therefore, it cannot reliably predict the airflow stability or the magnitude of the compression effect occurring along the blade span. This is particularly critical as rotor tip and stator hubs are prone to experiencing boundary layer detachment and flow reversal, as flow turning and centrifugal effect increase at higher radii [26]. Moreover, the RRM precluded the existence of radial velocity and momentum components, which must exist as the flowtrack converging geometry will naturally impose changes in radial coordinates [25]. Thus, it is necessary to expand the analysis to integrate these effects to the modelling through the TFM.

While the RRM solves the flow equations on cylindrical coordinates, the TFM is set up using the natural coordinates system, with the following mutually orthogonal components: streamwise ($m$), normal ($n$) and tangential ($\theta$). This change in coordinates considerably simplifies the flow equations, as the nodes (where mass, energy and momentum balance equations are evaluated) are located along streamlines. This ensures that, according to the streamline definition, no normal velocity component exists on the nodes, *i.e.*, $\vec{V}_n = 0$ [42]. Therefore, the absolute and relative velocity vectors on any given node are given by:

$$\vec{C} = V_m \vec{i}_m + C_\theta \vec{i}_\theta,$$
$$\vec{V} = V_m \vec{i}_m + (U - C_\theta) \vec{i}_\theta,$$

since $\vec{V}_m = \vec{C}_m$. The radial stations located between blade rows, as well as along the IGV inlet ($i = 0$) and OGV outlet ($i = \mathcal{S}$), are discretised into $\mathcal{N}$ nodes (Fig. 3(a)), located along streamlines which, when revolved around the axial direction $+z$, results in concentric stream-surfaces. The region encompassed between adjacent stream surfaces is the stream sheet. The generation of stream surfaces is schematically represented in Fig. 3(b). The velocities and flow angles considered in the TFM are depicted in Fig. 3(c), and are evaluated on all nodes.

The assumptions and simplifications used in the TFM are outlines and discussed ahead:

(B.1) Air is treated as a dry, ideal gas;
(B.2) Flow is adiabatic;
(B.3) Quasi-steady state;
(B.4) Inviscid flow;
(B.5) Nodes are located along stream surfaces;
(B.6) Aero-thermodynamic properties vary linearly between adjacent nodes;
(B.7) Axisymmetric flow with respect to $+z$;

Assumptions (B.1) through (B.4) are carried over from the RRM approach. Assumption (B.5) ensures that the mass flow rate carried by a stream sheet is constant from inlet to outlet, as well as setting $V_n = 0$ on all nodes. The nodes position will first be estimated, and then repositioned corrected until they are located on streamlines. Assumption (B.6) is used to reposition nodes, and is applied to Eq. (33). Finally, (B.7) states that in a given radial station, all nodes along the same stream surface are subjected to equal flow conditions, and thus, no preferential tangential position or gradients exist ($\partial/\partial\theta = 0$). Following, the key equations and concepts will be presented. The full derivation can be found in [26,29].

The differential mass flow rate continuity applied to each node is described by Eq. (32), while its integral form applied to any two adjacent nodes $N_1$ and $N_2$, positioned on the radial coordinates $r_1$ and $r_2$ respectively, is given by Eq. (33).

$$\frac{\partial r \rho V_m}{\partial m} + r \rho \kappa_n V_m = 0, \tag{32}$$

$$\dot{m}_{N_1 \rightarrow N_2} = 2\pi \int_{r_1}^{r_2} r \rho V_m \cos\phi dr, \tag{33}$$

In Eq. (32), $\kappa_n$ is the local stream surface curvature on the normal direction, $\rho$ and $V_m$ are the static density and streamwise velocity evaluated at the node, whose radial position is $r$. In Eq. (33), it is assumed that $V_m(r)$, $\rho(r)$ and $\phi(r)$ vary linearly between $r_1$ and $r_2$ (B.6).

The momentum equation for inviscid flow under a rotating frame of reference is presented in Eq. (34) [42]

$$\frac{D\vec{V}}{Dt} + 2\left(\vec{\omega} \times \vec{V}\right) + \vec{\omega} \times (\vec{\omega} \times \vec{r}) = T\nabla s - \nabla h \tag{34}$$

Here, $D\vec{V}/Dt$ is the material derivative of the velocity, $\vec{\omega} = \omega \vec{i}_z$ is the angular velocity vector, and $\nabla s$ and $\nabla h$ are the specific entropy and enthalpy gradients, respectively. Evaluating Eq. (34), combining it with Eq. (32) and imposing the assumptions (B.1) through (B.7), the streamwise momentum equation along a *quasi-normal* (Eq. (35)) is obtained.

$$V_m \frac{dV_m}{dy} = \left(\frac{dI}{dy} - T\frac{ds}{dy}\right) - V_m^2 \left\{ \kappa_m \cos\phi + \frac{1}{1 - Ma_m^2} \times \left[\left(1 + Ma_{C_\theta}^2\right) + \frac{\kappa_y}{\cos\phi} + \kappa_m \tan\phi\right]\right\} - \frac{V_\theta}{r}\frac{drC_\theta}{dy}, \tag{35}$$

where $y$ corresponds to the local quasi-normal coordinate in $m$, so that ($r = r_{hub} \implies y = 0$ and $dr = dy$, see Fig. 3(b)), $I$ is the specific rothalpy in J kg$^{-1}$, $\kappa_m$ and $\kappa_y$ are the stream surface streamwise and *quasi-normal* curvatures in m$^{-1}$, respectively. $Ma_m$ and $Ma_{C_\theta}$ are the streamwise and absolute tangential Mach numbers (*i.e.*, $V_m/SS$ and $C_\theta/SS$) respectively. The rothalpy $I$ is defined as the stagnation enthalpy under a rotating frame of reference, [26,42] and can be calculated by Eq. (36) while the stream surface streamwise and *quasi-normal* curvatures are calculated with Eqs. (37) and (38), respectively.

$$I = h_{\emptyset} - UC_\theta = h_{\emptyset R} - \frac{1}{2}U^2 \tag{36}$$

$$\kappa_m = -\frac{\partial \theta}{\partial m} \tag{37}$$

$$\kappa_y = \frac{\partial \theta}{\partial y} \tag{38}$$

It is assumed that rothalpy is conserved between nodes along the same stream surface across a blade row [26,42]. This allows calculating static and dynamic thermodynamic properties on all nodes along a *quasi-normal* given the blade row inlet aero-thermodynamic properties and the outlet velocities. Calculating this velocity profile requires solving the streamwise momentum equation and designing the blades to receive a given tangential velocity at inlet. This paper assumes vortex-free tangential velocities, Eq. (39)

$$rC_{\theta,in} = k \tag{39}$$

where $k$ is a constant calculated on all stations on the reference radius node (from RRM), using the dimensionless design parameters evaluated at $r = r_{ref} \implies (\varphi, \psi, \mathcal{R})_{ref}$ with Eq. (22). Following, the absolute and relative (rotors only) tangential velocity components are calculated for all remaining nodes on the *quasi-normal* through Eq. (39) along the blade row inlet. Then, the absolute outlet tangential velocity distribution, along station $i$ on stage $sg$, from nodes $1 \leqslant N \leqslant \mathcal{N}$ is determined from Eq. (40), manipulating the dimensionless design coefficients $(\varphi, \psi, \mathcal{R})$ and Eq. (39)

$$\begin{cases} C_{\theta 2,N,sg} = \dfrac{r_{1,N,sg}C_{\theta 1,N,sg} + \psi_{ref,sg}U_{1,ref,sg}r_{1,ref,sg}}{r_{2,N,sg}} & \text{rotors outlet,} \\ C_{\theta 3,N,sg} = U_{1,N,sg+1}\dfrac{r_{3,ref,sg}}{r_{3,N,sg}}\left(1 - \mathcal{R}_{ref,sg+1} - \dfrac{\psi_{ref,sg+1}}{2}\right) & \text{stators outlet,} \end{cases} \tag{40}$$

### 3.2.1. Geometry discretisation and update

The discretisation process purpose is to define the nodes locations, wherein the velocities, thermodynamic properties and streamlines geometries are calculated. The discretisation process also couples the preliminary geometry resultant of the RRM to the TFM. This greatly improves the speed at which the TFM achieves convergence. Along each station, $\mathcal{N}$ nodes are positioned as to equally divide the annulus into $\mathcal{N} - 1$ areas. By setting $\mathcal{N}$ as an odd number, then there will be a node (whose index is $\lceil \mathcal{N}/2 \rceil$) located on the reference radius. This spacing yields in equal mass flow rate on all stream sheets, recalling that the flow is considered uniform along the IGV inlet station. Once all stations have been divided, the nodes sitting on a given stream surface along all stations are fit via a Piecewise Cubic Hermite Interpolating Polynomial [57], which allows the calculation of the local stream surface angle $\phi$ for all nodes.

During the solution process, either in on- or off-design conditions, the nodes are be repositioned to ensure they are located along a stream surface. Therefore, as the node radial position changes, so will the stream surface angle $\phi$. However, within a given solution run (SR) step (*i.e.*, velocities and aero-thermodynamic properties calculation process from inlet to outlet), the stream surface angles are assumed constant on all nodes. After all stations have been analysed, the updated radial position is calculated and fed back into the discretisation algorithm to generate updated $\phi$ values, and the solution run (SR = SR + 1) restarts. This is iteratively repeated until a node position change residual tolerance criterion has been met. When the on-design analysis is underway, the geometry discretisation process also updates the hub and/or shroud contour positions, generating the final compressor geometry. Conversely, during the off-design, analysis, these are locked and only the nodes repositioning takes place.

### 3.2.2. Off-design performance and stability prediction

Once the on-design geometry and performance have been defined, the off-design analysis can take place. It is necessary to define a pair of off-design operating conditions, *i.e.,* mass flow rate and rotational frequency $[\dot{m}, \omega]^{OFF}$, to be analysed. Then, the discretisation process takes place on the established compressor geometry, leading to the definition of blade tangential velocity and stream sheet mass flow rate. The IGV behaviour must now be considered, for which there are two main options: fixed or adjustable. In the former, the IGV will receive and deliver the airflow with the same flow angles regardless of the off-design condition (assuming flow turning is independent of the velocity ratio [54]), which can lead to acute performance drop in far rotational speed off-design conditions. This paper assumes adjustable IGV that deliver the air at the design incidence angle to the first rotor row (station $i = 1$), as long as the flow stability check does not indicate that the required flow turning lead to unstable conditions.

he off-design performance requires a slight modification to Eq. (35), expressing the outlet velocity profile in terms of the flow angle instead of the tangential velocity components. As the dimensionless design coefficients cannot be applied in off-design conditions, the outlet tangential velocities (Eq. (40)) cannot be directly calculated. The flow angles, on the other hand, are determined as a function of the absolute incidence angle departure, $\delta\imath = |\imath^{OD} - \imath^{OFF}|$, local blade solidity $\sigma$ and the flow turning departure, $\delta\epsilon = f(\delta\imath)$, as reported in the charts developed by Lieblein in [55]. The modified streamwise momentum equation is presented in Eq. (41).

$$\begin{cases} \dfrac{dV_m}{dy} = V_m\left[\cos^2\beta\left(\dfrac{\sin\phi}{V_m}\dfrac{\partial V_m}{\partial m} - \dfrac{\tan\beta}{r}\dfrac{d(r\tan\beta)}{dy} - \kappa_m\cos\phi\right)\right] \\ \qquad\qquad + \omega\sin 2\beta + \left[\cos^2\beta\left(\dfrac{dI}{dy} - T\dfrac{ds}{dy}\right)\right]\dfrac{1}{V_m} \\ \dfrac{\partial V_m}{\partial m} = \dfrac{-V_m}{1 - Ma_m^2}\left[\left(1 + Ma_{C_\theta}^2\right) + \dfrac{\kappa_y}{\cos\phi} + \kappa_m\tan\phi\right] \end{cases} \tag{41}$$

The general solution procedure for off-design conditions is the same as for on-design operation. For a given pair of off-design operating conditions, $(\dot{m}, \omega)^{OFF}$, the off-design TFM analysis begins at step [TFM.2] –see Supplementary Material for the step-by-step application guide–, and carries on with steps [TFM.3] and [TFM.5] (Sec. SM.2). In substep [OS.5], Eq. (41) is used instead of Eq. (35). Within substep [OS.7], the node repositioning fixes nodes 1 (hub) and $\mathcal{N}$ (tip), as the compressor geometry has been defined in the design process. Also, the flow stability, [OS.8], checks if the chosen off-design operating conditions can be achieved by the compressor, by checking all inequalities in Eq. (42). If the chosen pair of off-design operating conditions, $[\dot{m}, \omega]^{OFF}$ does not trigger any stability checks, the compressor performance is calculated, [TFM.5], and stored. By exploring a range of off-design conditions, the operation limits are determined and the performance map is constructed.

### 3.2.3. Flow conditions check

A flow condition is considered stable if, on all nodes (or on $r_{ref}$ when the RRM procedure is taking place), the inequalities presented in

$$\left\{\begin{bmatrix}\omega_1\\ \omega_2\\ \vdots\\ \omega_{L_{\omega-1}}\\ \omega_{L_\omega}\end{bmatrix},\begin{bmatrix}\dot{m}_1\\ \dot{m}_2\\ \vdots\\ \dot{m}_{L_{\dot{m}-1}}\\ \dot{m}_{L_{\dot{m}}}\end{bmatrix}\right\}^{OFF} \xrightarrow{outcome} \begin{bmatrix} (P_{out},\dot{W}_c,\eta_s)_{1,1} & (P_{out},\dot{W}_c,\eta_s)_{1,2} & \cdots & (failure)_{1,L_\omega-1} & (failure)_{1,L_\omega}\\ (P_{out},\dot{W}_c,\eta_s)_{2,1} & (P_{out},\dot{W}_c,\eta_s)_{2,2} & \cdots & (failure)_{2,L_\omega-1} & (failure)_{2,L_\omega}\\ (failure)_{3,1} & (P_{out},\dot{W}_c,\eta_s)_{3,2} & \cdots & (P_{out},\dot{W}_c,\eta_s)_{3,L_\omega-1} & (failure)_{3,L_\omega}\\ & \vdots & \ddots & & \vdots\\ (failure)_{L_{\dot{m}}-2,1} & (failure)_{L_{\dot{m}}-2,2} & \cdots & (P_{out},\dot{W}_c,\eta_s)_{L_{\dot{m}}-2,L_\omega-1} & (P_{out},\dot{W}_c,\eta_s)_{L_{\dot{m}}-2,L_\omega}\\ (failure)_{L_{\dot{m}}-1,1} & (failure)_{L_{\dot{m}}-1,2} & \cdots & (failure)_{L_{\dot{m}}-1,L_\omega-1} & (P_{out},\dot{W}_c,\eta_s)_{L_{\dot{m}}-1,L_\omega}\\ (failure)_{L_{\dot{m}},1} & (failure)_{L_{\dot{m}},2} & \cdots & (failure)_{L_{\dot{m}},L_\omega-1} & (P_{out},\dot{W}_c,\eta_s)_{L_{\dot{m}},L_\omega}\end{bmatrix}$$

**Box I.**

Eq. (42) are valid [26]:

$$\begin{cases}\dfrac{V_2}{V_1} < 0.72\\ DF \leqslant 0.6\\ DF_{EQ} < 2.2\\ \sqrt{\dfrac{P_{\emptyset R,2}-P_2}{P_{\emptyset R,1}-P_1}} < \dfrac{(0.15+11\mathbb{T}/\mathbb{C})/(0.25+10\mathbb{T}/\mathbb{C})}{1+0.4\left\{\theta\sigma/\left[2\sin(\theta/2)\cos\gamma_s\right]\right\}}\\ \dfrac{\theta\sigma}{2\sin(\theta/2)\cos\gamma_s} \geqslant 1.1\\ \zeta_P^{OFF} < 2\zeta_P^{ON}\\ Ma_C < 1\\ Ma_V < 1\end{cases} \tag{42}$$

where $\mathbb{T}/\mathbb{C}$ is the blade relative thickness, equal to 0.10 for the NACA 6510 blade series [53], $\theta$ is the blade camber angle in radians and $\gamma_s$ is the blade stagger angle. Aungier [26] also limits the application of the stability correlations (Eq. (42)) to off-design rotational speeds greater than 85% of the design value, as below this threshold the inviscid flow assumption loses accuracy due to greater relative importance of viscous effects. For the RRM, only the first three inequalities are checked, whereas on-design TFM checks for the first five. When the off-design TFM takes place, all conditions established in Eq. (42) must be met. In Eq. (42), the conditions checked include localised stall, surge and chocked flow. In the case of the RRM and on-design TFM, a failure to fulfil any of the inequalities in Eq. (42) results in updating the design parameters, whilst when the off-design TFM is taking place, it represents an unstable off-design operating conditions pair $[\dot{m},\omega]^{OFF}$, and thus, is not included in the compressor map.

#### 3.2.4. Global solution run: Off-design

The global solution run in off-design conditions is different to the on-design since no geometry update takes place. Therefore, no iterative solution convergence process is necessary. However, it is necessary to test numerous off-design operating conditions to identify the stable margins and performance figures. For a given pair of inputs $[\dot{m},\omega]^{OFF}$, there are two possible outcomes: a failure to operate at these conditions or the return of performance indicators of outlet pressure, power consumption and isentropic efficiency, $[P_{out},\dot{W}_c,\eta_s]^{OFF}$. Assuming $L_{\dot{m}}$ and $L_\omega$ are the number of off-design mass flow rates and rotational speeds scenarios analysed, then the off-design global solution run possible outcomes are schematically represented as an $L_{\dot{m}}$ by $L_\omega$ performance matrix: (See the expression in Box I).

Once the performance matrix has been defined, it is possible to determine an operational strategy and so, propose functions which allow calculating the compressor instantaneous mass flow rate, rotational speed, power consumption and isentropic efficiency as a function of the outlet pressure, or $[\dot{m},\eta_s,\omega,\dot{W}_c]^{OFF} = f(P_{out})$. Such strategies can be, for instance, setting the rotational speed to reach the maximum efficiency, maximum power consumption or to meet a given external power availability. This way, the compressor design and performance prediction is coupled to the ACAES model by the instantaneous storage pressure.

## 4. Results

### 4.1. Compressor geometry and performance

The compressor design procedure began by choosing the key design parameters and variables, as described throughout Section 3, and applying them in the RRM, which yielded preliminary flow conditions and geometry (i.e., flowtrack contour and number of stages), allowing a qualitative and quantitative analysis of the performance and flow stability (via $DF$ and $DF_{EQ}$). Moreover, the RRM was instrumental in building an understanding on how changing a dimensionless design coefficient affected the overall stability and geometry. It was quickly noticed that even if conservative values for $\varphi,\psi,\mathcal{R}$ were chosen, following general recommendations and guidelines in literature [25,26,41,44], stability issues or unsatisfactory performance were common outputs. Due to the high pressures generally involved in ACAES storage (see Section 4.2), the axial-flow compressor was split into two spools capable of rotating at different speeds, with an intercooler in between. It is noteworthy that, despite the distinct rotational speeds of the two spools, any adjustments to their rotational frequencies are inherently synchronised due to their mechanical coupling. Consequently, independent rotation of the spools is not possible. Table 3 lists the design values and parameters, used in both RRM and TFM.

In Table 3, the design outlet stagnation pressure corresponds to the second spool outlet stagnation pressure, later recovered as static pressure in the second diffuser. The faster rotational speed in second spool is to mitigate the decreased centrifugal effect caused by the lower reference radius, which in turn, occurs to avoid excessively low blade heights, $\mathbb{H}$ – given that the cross section flow area decreases to accommodate the increasing air density. The design mass flow rate was chosen at 100 kg $s^{-1}$, a similar value to Huntorf and McIntosh plants [10], whilst the design rotation speeds were chosen as 1.5 and 3 times the UK synchronous frequency — first and second spool respectively. The Reference radii in each spool were chosen to keep the blade speed below sonic in front stages whilst checking the resultant axial velocity via the flow coefficient. The blade aspect ratio in each spool was first estimated based on [45], and then manually adjusted until a reasonable compromise between blade height and number of stages was achieved. The RRM results generated the preliminary geometry, *i.e.*, the number of stages and flow track contours ($r_{hub}$ and $r_{tip}$) to be used in the TFM analysis. Although the RRM is capable of outputting performance figures, both in on- and off-design conditions, these results were found to be unreliable when compared to the TFM. The first spool comprises of 18 stages, spanning approximately 2 m in total length and blade height decreasing from $\mathbb{H} \approx 0.2$ m at the IGV inlet down

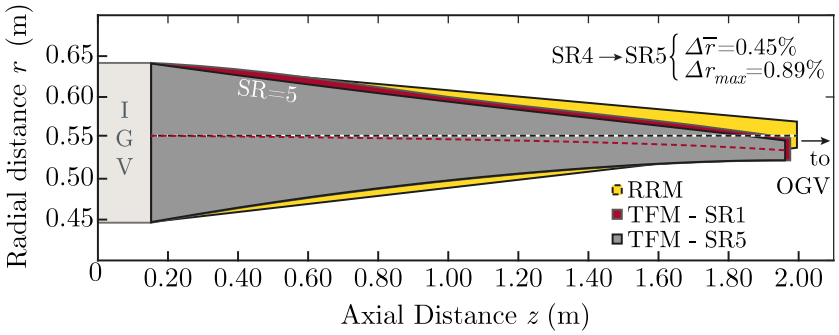


**Fig. 4.** Spool 1 geometry: In yellow, the RRM preliminary geometry with constant reference radius (B&W dashed line); in red, the first solution run iteration (SR = 1), already depicting significant changes to the RRM design, and; in grey, the fifth and final TFM solution run, showing the definitive compressor geometry. Note that the constant reference radius assumption is not enforced in the TFM, leading to a decrease the reference radius (red dashed line). In the upper right corner, the mean and maximum relative node radial coordinate change from solution runs 4 to 5 indicate a stable geometry.

**Table 3**
Key compressor design values and dimensionless parameters.

| Variable | Symbol | Value | Unit |
|---|---|---|---|
| Mass flow rate | $\dot{m}^{OD}$ | 100 | kg s$^{-1}$ |
| Outlet stagnation pressure[a] | $P^{OD}_{\emptyset,out}$ | 7.2 | MPa |
| Rotational speed (spool 1) | $\omega^{OD}_{SP1}$ | 4500 | rpm |
| Rotational speed (spool 2) | $\omega^{OD}_{SP1}$ | 9000 | rpm |
| Blade aspect ratio (spool 1) | $\Lambda_{SP1}$ | 1.35 | – |
| Blade aspect ratio (spool 2) | $\Lambda_{SP2}$ | 1.0 | – |
| Blade profile | – | NACA 6510 | – |
| Blade solidity[b] (spool 1, rotors) | $\sigma_{SP1,R}$ | 1.225 | – |
| Blade solidity (spool 1, stators & guide vanes) | $\sigma_{SP1,S}$ | 1.125 | – |
| Blade solidity (spool 2, rotors) | $\sigma_{SP2,R}$ | 1.3 | – |
| Blade solidity (spool 2, stators & guide vanes) | $\sigma_{SP2,S}$ | 1.3 | – |
| Reference radius (spool 1) | $r_{ref,SP1}$ | 0.55 | m |
| Reference radius (spool 2) | $r_{ref,SP2}$ | 0.20 | m |
| Flow coefficient | $\varphi$ | 0.55 | – |
| Load coefficient | $\psi$ | 0.35 | – |
| Degree of reaction | $\mathcal{R}$ | 0.50 | – |
| Number of nodes per *quasi-normal* | $\mathcal{N}$ | 21 | – |

[a] Target
[b] All solidities values for the reference radius node.

to $\mathbb{H} \approx 0.05$ m at the OGV outlet. The second spool is shorter, spanning 0.8 m in length, in which there are 15 stages at an outlet-to-inlet cross section area ratio equal to 0.34. Fig. 4 shows the first spool geometry resultant of the analysis: (1) in yellow, the solution obtained from the RRM, with the constant reference radius depicted in a black-and-white dashed line; (2) in red, the first solution obtained from the TFM (SR1) and finally, (3) the definitive geometry after 5 iterations (SR5, see Sec. SM.2), whose reference radius is represented by the red dashed line.

It is noticeable in Fig. 4 that the RRM was able to output an acceptable preliminary geometry, enabling the TFM to be run for only five SR iterations before the geometry settles. Note that in the TFM, the reference radius is allowed to change. On the top right, the mean and maximum relative node position change between solution runs SR 4 and 5 is indicated. The length shortening observed in Fig. 4 is due to the blade height decrease at constant blade aspect ratio, leading to a smaller blade chord length.

When operating on-design conditions (100 kg s$^{-1}$, 4500 rpm), the first compressor spool is able to reach an outlet stagnation pressure and temperature equal to 1.75 MPa and 671.7 K (≈400 °C), consuming 41.2 MW at an overall stagnation isentropic efficiency of 93%. The second spool, also on-design conditions (100 kg s$^{-1}$, 9000 rpm), is responsible for the remaining compression, delivering the airflow at a stagnation pressure and temperature equal to 7.29 MPa and 473.6 K (≈200 °C), at a slightly lower efficiency of 90%, consuming 18 MW. Note that the actual outlet pressure is slightly higher than the target design value, due to the discrete nature of pressure increase over a blade row. Also, the asymmetric compression is justified by the need to preserve the highest possible coolant temperature, and therefore, ensuring appropriate heating prior to the expanders [11]. The Highest outlet temperature indicates that the compressor can be built from special steel alloys, such as ASTM A 216, grade WCB [58] or ASTM A 470, class 7 [59]. The compressor design performance is summarised in Table 4

**Table 4**
On-design Throughflow Method (TFM) - overview of the results.

| Property | Symbol | Value | | | Unit |
|---|---|---|---|---|---|
| | | 1st spool | 2nd spool | Total | |
| Number of stages | – | 18 | 15 | 33 | – |
| Power consumption | $\dot{W}$ | 41.2 | 18 | 59.2 | MW |
| Stagnation isentropic efficiency | $\eta_s$ | 0.93 | 0.90 | 0.92 | – |
| Outlet stagnation pressure | $P_{\emptyset,out}$ | 1.75 | 7.29 | 7.29 | MPa |
| Outlet stagnation temperature | $T_{\emptyset,out}$ | 671.7 | 473.6 | 473.6 | K |

Once the on-design analysis is complete, the compressor geometry is locked and used to calculate the off-design performance and safe operational limits. Twelve off-design mass flow rate and rotational speed values, ranging from 80% up to 110% of the design value, were tested, totalling 144 possible operating points. It was expected, as discussed in Section 3.2.3, that far off-design operating conditions would fail the stability assessment. All rotational speeds below 85%$\omega^{OD}$ failed the stability check, as predicted in [26]. On the opposite end of the off-design velocity, all speeds over 105% also failed the stability check. This narrow off-design operating range is expected, as the off-design flow turning effects stacks over the numerous stages, monotonically increasing the incidence angle departure across the blade rows. Results suggest the compressor successfully delivered air at the appropriate pressure range required in the case-study ACAES system, $5.80 \leqslant P_{\emptyset,out} \leqslant 8.10$ MPa (taking into account the 5% aftercooler AC pressure drop). The compressor operating map is depicted in Fig. 5. The stable outlet pressures at specified speeds were obtained as a combination of two factors: (*i*) The high number of stages (33) spread out the off-design effect on each stage, which in turn, decreases the performance penalty and (*ii*) the variable IGV on each spool delivering the airflow at the incidence angle to the first rotor row significantly decreases the incidence angle departure, which also improves the off-design performance. However, it is expected that once further research is conducted, particularly with the implementation of viscous models and CFD analysis, the off-design penalty will become more prominent. Furthermore, the high number of stages narrows the operation range, particularly in light of the 6th check in Eq. (42), *i.e.*, $\zeta_P^{OFF} < 2\zeta_P^{ON}$. In the analysis of far-off design conditions, the incidence angle departure increases rapidly, leading to a significant increase in the loss coefficient, and a major decrease in performance and outlet pressure. Given the compressor application in

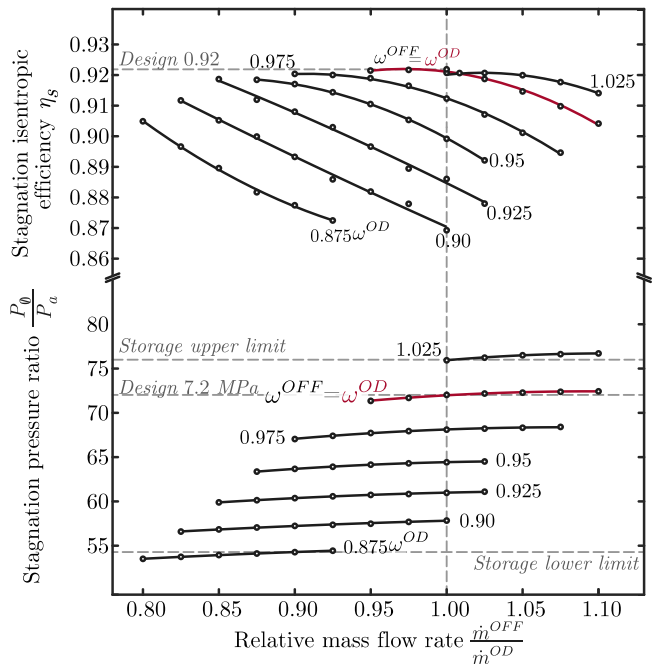


**Fig. 5.** Axial-flow compressor stable operating map. The red line indicates the design rotational speed, highlighted for ease of visualisation. Markers indicate a valid result from the off-design TFM, while solid line corresponds to a second-degree curve fitting at a constant, off-design rotational speed. **Top:** Overall (first spool inlet to second spool outlet) stagnation isentropic efficiency; **Bottom:** Second spool outlet stagnation pressure ratio. In both plots, the results are depicted for various off-design rotational speeds at the off-design mass flow rate range.

ACAES, wherein the need to maintain high isentropic efficiency has been postulated as a design prerequisite, such points are not included in the performance map.

To implement the generated compressor map into the ACAES model, it is necessary to determine an operation strategy. This way, the instantaneous storage pressure $P_{HPST}(t)$ is used to determine the instantaneous stagnation pressure ratio, $P_\emptyset/P_a$, in which the compressor outlet stagnation pressure is $P_{\emptyset,out} = P_{HPST}(t)/0.95$, where the factor in the denominator is due to the IC/AC pressure drop. Then, taking the imposed stagnation pressure ratio, the off-design mass flow rate and rotational speed are selected as to reach the maximum isentropic efficiency. For instance, an overall stagnation pressure ratio of 65 (see Fig. 5, bottom) could be reached by the compressor operating at rotational speeds between 95 and 97.5%$\omega^{OD}$ and off-design mass flow rate between 0.875 and 1.05$\dot{m}^{OD}$. At these rotational speeds, the highest efficiency levels (see Fig. 5, top) are obtained around the lowest off-design mass flow rate, leading to $\omega^{OFF} \approx 0.965\omega^{OD}$ and $\dot{m}^{OFF} \approx 0.89\dot{m}^{OD}$. Therefore, the instantaneous compressor mass flow rate, isentropic efficiency and rotational speeds are fully determined by the storage pressure, *i.e.,* $[\dot{m}, \omega, \eta_s](t) = f(P_{HPST}(t))$.

### 4.2. System performance

The system performance is analysed under continuous cycling, until it reaches equilibrium conditions [6]. Table 5 summarises the ACAES components key operational parameters used in the analysis.

The High Pressure Store, HPST, is considered adiabatic during system charge and discharge. Conversely, between consecutive charging and discharging periods (idle) or discharging and charging (recovery), it is assumed that enough time elapses to allow the stored air to reach thermodynamic equilibrium with the storage and ambient, cooling (idle) or heating up (recovery) isochorically until $T_{HPST} = T_a$. The throttle is assumed isenthalpic.

**Table 5**
Key compressor design values, dimensionless parameters and resulting operating ranges for proposed system. Ranges correspond to initial and final values. For reference, see Fig. 1.

| Variable | Symbol | Value | Unit |
|---|---|---|---|
| *Ambient*: | | | |
| Temperature | $T_a$ | 298.15 | K |
| Pressure | $P_a$ | 101.325 | kPa |
| *HPST*: | | | |
| Volume | $V_{HPST}$ | $3 \cdot 10^5$ | $m^3$ |
| Pressure (minimum) | $P_{HPST,min}$ | 5.5 | MPa |
| Pressure (maximum) | $P_{HPST,max}$ | 7.7 | MPa |
| Pressure (throttle) | $P_{thr}$ | 5.3 | MPa |
| Heat exchangers regime: | | | |
| Charging and Discharging | | Adiabatic | |
| Idle and Recovery | | Isochoric, until $T_{HPST} = T_a$ | |
| *Heat exchanger (IC and AC)*: | | | |
| Coolant fluid | – | Dowtherm A | [32] |
| Fluid temperature range | – | 288.15–673.15 | K |
| Pressure drop - air | $\Delta P_{air}$ | $0.05P_{air}^{in}$ | MPa |
| Inlet temperature - air | $T_{air}^{in}$ | IC: 518.7–659.1<br>AC: 438.8–467.1 | K |
| Inlet temperature - coolant | $T_{cool}^{in}$ | 298.15 | K |
| Outlet temperature - air | $T_{air}^{out}$ | 313.15 | K |
| Outlet temperature - coolant | $T_{cool}^{out}$ | IC: 484.4–606.9<br>AC: 415.9–442.9 | K |
| Mass flow rate - Coolant | $\dot{m}_{cool}$ | IC: 56.1–68.2<br>AC: 52.4–60.7 | kg $s^{-1}$ |
| Heat capacity ratio | $C_r$ | 0.9 | – |
| *Expanders*: | | | |
| Mass flow rate | $\dot{m}_{dis}$ | 90 | kg $s^{-1}$ |
| Inlet Pressure - expander 1 | $P_{ex1}^{in}$ | 5.0 | MPa |
| Expansion ratio - expander 1 | $PR_{ex1}$ | 7.5 | – |
| Inlet pressure - expander 2 | $P_{ex2}^{in}$ | 638 | kPa |
| Expansion ratio - expander 2 | $PR_{ex2}$ | ≈6.3 | – |
| Isentropic efficiency | $\eta_s$ | 0.9 | – |
| *Heat Exchanger (Heaters)*: | | | |
| Mass flow rate | $\dot{m}^{dis}$ | 90 | kg $s^{-1}$ |
| Coolant fluid | – | Dowtherm A | [32] |
| Fluid temperature range | – | 288.15–673.15 | K |
| Pressure drop - air | $\Delta P_{air}$ | $0.05P_{air}^{in}$ | MPa |
| Inlet temperature - air | $T_{air}^{in}$ | H1: 294.5–280.7<br>H2: 309.2–308.7 | K |
| Inlet temperature - coolant | $T_{cool}^{in}$ | H1: 555.5 // H2: 431.1 | K |
| Outlet temperature - air | $T_{air}^{out}$ | H1: 541.5–540.8<br>H2: 424.1–424.0 | K |
| Outlet temperature - coolant | $T_{cool}^{out}$ | H1: 333.1–321.4<br>H2: 327.6–327.3 | K |
| Mass flow rate - Coolant | $\dot{m}_{cool}$ | H1:51.7// H2: 48.7 | kg $s^{-1}$ |
| Heat capacity ratio | $C_r$ | 0.9 | – |

The system reaches equilibrium after 5 charge–discharge cycles, defined as when two consecutive round-trip efficiencies do not vary by more than ±0.1%. In equilibrium conditions, the charging and discharging process take approximately 15 h each to be completed, wherein the ACAES system consumes 757 MWh in the compressors and returns 529.5 MWh in the expanders (no electric motor and generator inefficiencies are considered), yielding a round-trip efficiency of 70%. Fig. 6 depicts the evolution of energy consumption and generation, as well as round-trip efficiency and run-time from cycles 1 through 5, when the system stability was achieved.

In Fig. 6, the first cycle performance is significantly inferior to subsequent cycles, as reported in [6]. This is a result of the first cycle initial storage conditions ($P = P_{HPST,min}, T = T_a$) not matching the conditions encountered at the end of the recovery period. This leads to an imbalance in mass flow added and removed from the HPST on the first few cycles, quickly settling by the fifth run. Concurrently, the mass imbalance leads to lower round-trip efficiency, since part of the mass compressed does not flow past the expanders. Once the system reaches

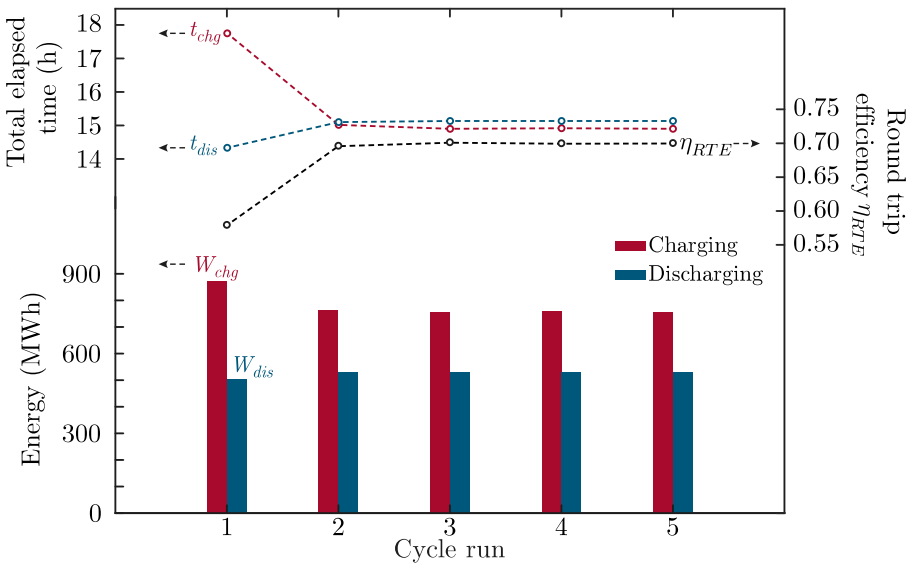


**Fig. 6.** Composite plot depicting the system cycle performance until stability is reached, after 5 global runs. **Bottom:** bars indicating the total energy consumption and generation during charging and discharging, respectively. **Top:** the black dots indicate each cycle run RTE, whilst the red and blue dots correspond to each cycle run elapsed time.

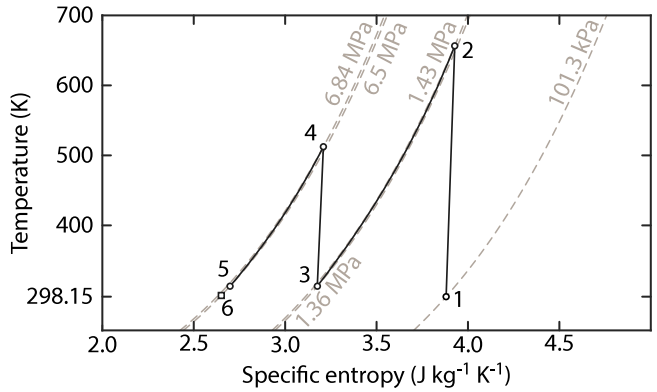


**Fig. 7.** Charging components represented in a T-s diagram for a storage pressure equal to 6.5 MPa. Indices 1 through 6 correspond to the presented in Fig. 1, namely (1) compressor inlet and stagnation ambient conditions, (2) first spool outlet and intercooler inlet, (3) intercooler outlet and second spool inlet, (4) second spool outlet and aftercooler inlet, (5) aftercooler outlet and (6) HPST condition.

equilibrium, the final recovery and initial charging processes pressures will become equal. The model round-trip efficiency resulting value is in accordance with numerous published results [22,27,60]. Crucially, the compressor model is linked to an actual geometry for an axial machine, which has been designed based on its impacts on the remaining components given ACAES technical challenges and constraints [11]. Fig. 7 depicts the thermodynamic properties on the compression train for a representative instant in the charging process, randomly chosen when the storage pressure equals 6.5 MPa.

In Fig. 7, the charging side of the proposed ACAES system is depicted in a T-s diagram, for when the storage pressure equal 6.5 MPa. The near-vertical lines correspondent to the compressor operation (1–2 and 3–4) are indicate of the spools high isentropic efficiency, approximately 90% in each spool. Moreover, the inter- and aftercooler 5% pressure drop results in a slight entropy increase when compared to the isobaric operation. Fig. 8 depicts the storage behaviour for the 5$^{TH}$ cycle run.

In Fig. 8, the storage pressure and temperature during the four key periods of the ACAES operation cycle are depicted. During the system charging, air flow into the HPST compresses stored air, increasing the storage overall temperature, as predicted in [6] and experimentally verified in [18]. Similarly, the outflowing air during the discharge decreases the storage pressure and temperature. Isochoric cooling down to ambient temperature occurs during the idle period and the idle cooling heat flow ($Q_{idle}$) can, therefore, be considered a loss. On the other hand, the recovery period after discharging increases the storage temperature back to ambient conditions, and as such, $Q_{rec}$ can be considered an energy gain. The combined effect of heat flow in idle and recovery periods results in a net loss of energy, since the idle heat rejection occurs when the stored air mass is at its maximum whereas the recovery takes place when the stored air mass is at its lowest, *i.e.*, $|Q_{idle}| > |Q_{rec}|$. Fig. 8 also shows that since the charging process is complete when the storage pressure reaches the maximum allowable value, the storage period (idle) will always lead to lower starting storage pressure without compensation. Likewise, the initial charging pressure will be higher than the minimum storage pressure as a result of the recovery period pressure gain. Fig. 9 will now investigate the work flow in the turbomachinery - compressors and expanders.

In Fig. 9, the red lines correspond to the compressor variables, whilst the blue ones represent the expanders. As the storage pressure increases during charging, the compressor rotational speed increases to be able to reach higher output pressures, consequently increasing the mass flow rate and power consumption. The compressor stagnation isentropic efficiency initially increases before plateauing at around 92%. The higher than usual efficiency values can be accredited to the inviscid model, which can overlook secondary flow and boundary layer losses [41]. Moreover, the semi-empirical models used for losses are obtained from low-speed linear cascade tests [54,55], and therefore, their use is limited to guidelines. As important as the value of efficiency, the compressor ability to maintain satisfactory performance in off-design operation is critical to ACAES. The hypothesis that the axial-flow compressor would perform well in off-design conditions, by spreading the off-design penalty over more stages and thus, decreasing the individual stage performance penalty has been confirmed by the TFM for inviscid adiabatic flow. Further studies to include viscous effects, CFD analysis and prototype experimentation are imperative though, and it is expected that the performance values will decrease when viscous effects are taken into account. On the other hand, by further investigating and optimising the compressor design, it is expected that the required number of stages will decrease significantly, leading to a wider operating window. The current analysis is, nevertheless, an

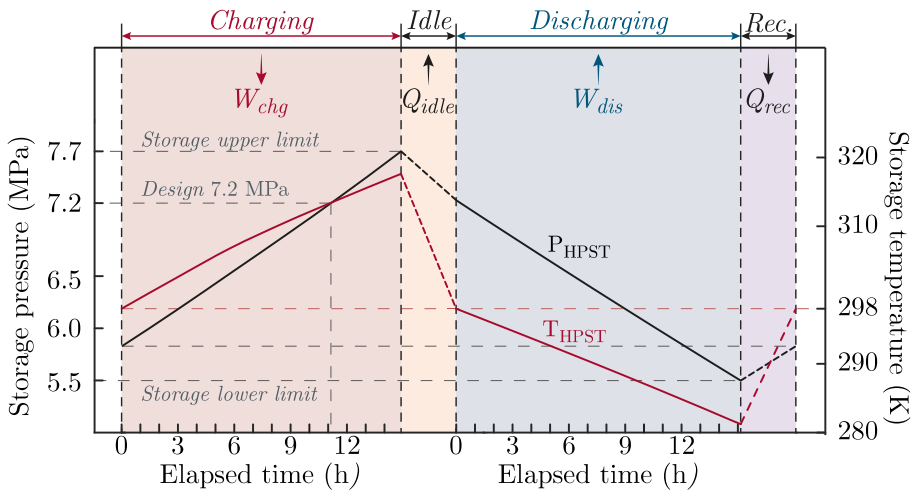


**Fig. 8.** Composite plot depicting the storage temperature and pressure in each of the four processes composing a cycle run. **Bottom:** pressure (black, LHS axis) and temperature (red, RHS axis) over the full 5TH cycle. The dotted lines during idle and recovery indicate that it is assumed that enough time elapses to achieve thermal equilibrium. **Top:** work and heat flows encompassing the ACAES plant.

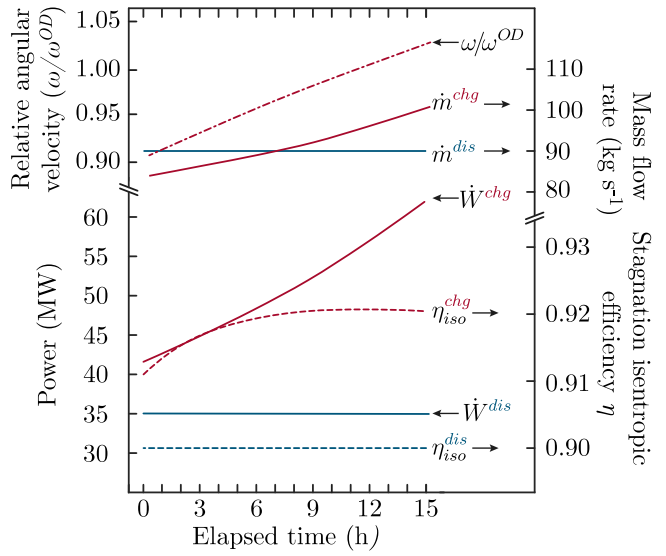


**Fig. 9.** Composite plot depicting the turbomachinery performance evolution during the system charging and discharging processes. **Bottom, RHS axis:** red and blue dotted line indicating the compressor and expander instantaneous isentropic efficiency, respectively; **Bottom, LHS axis:** red and blue solid lines corresponding to the compressor power consumption and expander power generation, respectively. **Top, RHS axis:** red and blue solid lines depicting the compressor variable and expander constant mass flow rates; finally **Top, LHS axis:** red dot-dashed line indicating the compressor instantaneous relative angular velocity.

important step in reassessing the compressor design and operation requirements in an ACAES context. The throttle valve presence in the HPST outlet regulates and maintains the discharging mass flow rate and pressure constant, leading to the horizontal lines depicted in Fig. 9. Finally, Fig. 10 depicts the heat flow in the heat exchangers, the TES tanks temperatures and state of charge (S.o.C) during the ACAES system charging and discharging processes.

Fig. 10, top, depicts the heat flow on the charging (IC and AC) and discharging (HE1 and HE2) heat exchangers. As expected, the discharging heaters exchangers provide heat at a virtually constant magnitude during the discharge process. There is a subtle increase in heat flow for both heaters to account for the storage temperature drop (Fig. 8), which then increases the required heat transfer from the TES into the airflow via HE1 and HE2. This effect is more prominent for HE1, as can be seen by the reference thin horizontal dotted line, given it is directly downstream the throttle valve. For the charging heat exchangers, on the other hand, the sliding storage pressure coupled with the increasing mass flow rate (see Figs. 8 and 9) results in a monotonically increasing heat transfer. As the first compressor spool and expander are subjected to the largest pressure change in their respective sections, the intercooler and HE1 will have greater absolute heat exchange rates than the AC and HE2, respectively. In terms of TES temperature, Fig. 10 mid section, it can be seen that the temperature decreases slightly during the first few hours into the charging period. This is due to the increasing compressor efficiency, particularly in the first spool, resulting in a decrease in spool outlet temperature despite the growing outlet pressure. After approximately four hours into charging, the relative magnitude of the pressure increase overtakes the efficiency increase, and the temperature slowly increases, as the thermal fluid outflowing the IC and AC mixes with previously stored fluid at lower temperature. During discharge, the temperature remains constant. Finally, the bottom portion of Fig. 10 simply depicts the state of charge of the TES systems, showing that under continuous cycling the thermal energy stored during charging is fully depleted during discharging.

Overall, the results can be considered promising, as the designed axial-flow compressor successfully addressed the charging–discharging coupling challenge, outputting air at higher than usual temperatures whilst maintaining the appropriate, high isentropic efficiency required. Albeit the inviscid flow simplification resulted in higher than expected efficiency, future works in the area can significantly benefit and build upon the principles developed in this paper. The methodology hereby presented bridges the *black-box* thermodynamic models, commonly reported in CAES literature, with highly specific aero-thermodynamic concepts and analysis, providing a solid framework to predict the compressor operation in ACAES contexts. It is recommended that, as initially proposed in [11], the same level of detail and scrutiny applied for the compressor is extended to turbines, heat exchangers and TES systems. ACAES imposes unique challenges, and the application-oriented design process must take these into account.

The authors are unaware of ACAES literature references which took the compressor design and performance prediction into such extent. Whereas the proposed design is able to reach the required discharge pressures whilst varying the mass flow rate and maintaining a high isentropic efficiency, the bespoke nature of the compressor geometry coupled to numerous application-oriented design choices indicate that

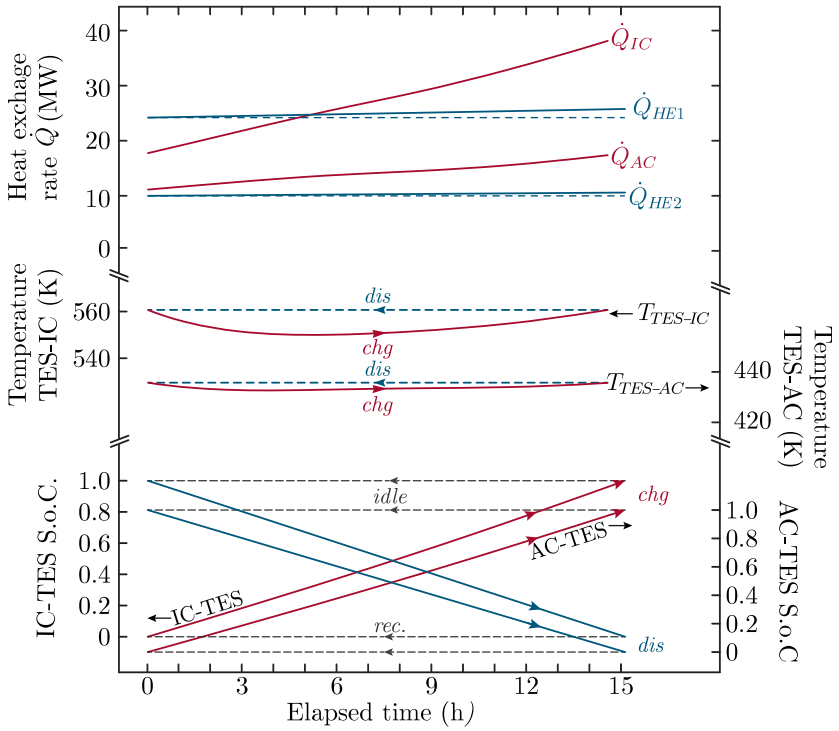


**Fig. 10.** Composite plot depicting the major heat flows, TES temperatures and state of charge (S.o.C.) during the 5TH cycle charging and discharging processes. **Bottom** red and blue lines depicting the S.o.C of the AC-TES (RHS axis) and IC-TES (LHS axis), during charging and discharging, respectively. In both cases, no changes are considered during idle and recovery. **Mid:** AC-TES (RHS axis) and IC-TES (LHS axis) temperature during charging and discharging. The initial drop in temperature observed in both cases is due to the greater effect of the increase in each spool isentropic efficiency when compared to the increasing overall pressure ratio, leading therefore, to lower outlet temperatures. **Top:** Heat exchange rate in the inter-and aftercooler (red), and heaters (blue) during charging and discharging, respectively. The blue dotted line are horizontal references to better illustrate a slight increase in thermal load during discharge, stemming from the decreasing storage temperature — see Fig. 8.

the thorough scrutiny applied in this paper must be extended and applied to detailed analysis of any ACAES system performance.

## 5. Conclusions

Thermodynamic analyses of ACAES system are widespread in technical literature. This paper extends the current state-of-the-art by integrating a thermodynamic model for an ACAES system with a model of a specifically-designed ACAES compressor, using the Reference Radius and Throughflow Methods. The designed compressor is a two-spool axial machine with an intercooler between each compression stage. The compressor performance map is generated and therefore for the first time in published literature the compressor performance map for an ACAES compressor is linked to a feasible compressor geometry. The designed compressor accounts for the particular needs of ACAES of preserving higher airflow temperature, whilst maintaining high efficiencies and ensuring flow stability.

The designed compressor performs satisfactorily in on- and off-design conditions, being able to mitigate the off-design penalty imposed by the variable storage pressure by spreading the changing conditions over 33 stages (across two spools) and implementing an adjustable rotational speed control. The requirement of preserving high temperature heat for the thermal storage lead to an unconventional geometry, which indicates that the bespoke design analysis is required for predicting performance in ACAES, as well as crucially to identify the stable operating limits. With the bespoke compressor design, a simulated ACAES system is able to reach a round trip storage efficiency in excess of 70%. Analogously to our use of the RRM to generate the input geometry for the TFM, the results of this paper can be used to initiate a more complex CFD analysis, providing an excellent jump-start to computationally-expensive numerical analysis and ultimately pavign the way for pilot system design. Overall, the developed methodology is a crucial step towards moving ACAES from a potential candidate to a widespread reality for economically-viable, grid-scale, energy storage.

## CRediT authorship contribution statement

**Daniel L. Pottie:** Conceptualization, Formal analysis, Investigation, Methodology, Resources, Software, Validation, Writing – original draft, Writing – review & editing. **Maury M. Oliveira Jr:** Formal analysis, Writing – review & editing. **Bruno Cardenas:** Writing – review & editing. **Zahra Baniamerian:** Writing – review & editing. **Seamus Garvey:** Writing – review & editing. **James Rouse:** Writing – review & editing. **Edward Hough:** Writing – review & editing. **Audrius Bagdanavicius:** Writing – review & editing. **Abdullah M. Ali:** Writing – review & editing. **Philip Eames:** Funding acquisition, Supervision, Writing – review & editing. **Edward R. Barbour:** Conceptualization, Funding acquisition, Project administration, Supervision, Writing – original draft, Writing – review & editing.

## Declaration of competing interest

The authors declare that they have no known competing financial interests or personal relationships that could have appeared to influence the work reported in this paper.

## Data availability

Data will be made available on request.

## Acknowledgements

This research was partly funded by the UK EPSRC grant number EP/W027569/1, Sustainable, Affordable and Viable Compressed Air Energy Storage (SAVE-CAES).

## Appendix A. Supplementary data

Supplementary material related to this article can be found online at https://doi.org/10.1016/j.enconman.2024.118233.

## References


[1] Nottingham University. Medium duration energy storage – kingpin of net zero energy. 2021, Accessed on Jan 29th, 2024. Available at https://www.nottingham.ac.uk/research/research-areas/energy-institute/news-and-events/news/medium-duration-energy-storage.aspx, Online.

[2] McNamara JW, DeAngelis V, Byrne RH, Benson A, Chalamala BR, Masiello R. Long-duration energy storage in a decarbonized future: Policy gaps, needs, and opportunities. MRS Energy Sustain 2022;6:142–70. http://dx.doi.org/10.1557/s43581-022-00037-9.

[3] Barbour ER, Pottie DL. Adiabatic compressed air energy storage systems. In: Cabeza LF, editor. Encyclopedia of energy storage. Oxford: Elsevier; 2022, p. 188–203. http://dx.doi.org/10.1016/B978-0-12-819723-3.00061-5.

[4] Akhil AA, Huff G, Currier AB, Kaun BC, Rastler DM, Chen SB, Cotter AL, Bradshaw DT, Gauntlett WD. DOE/EPRI 2013 electricity storage handbook in collaboration with NRECA. SAND2013-5131, Sandia National Laboratories; 2013.

[5] Borri E, Tafone A, Comodi G, Romagnoli A, Cabeza LF. Compressed air energy storage - An overview of research trends and gaps through a bibliometric analysis. Energies 2022;15(20). http://dx.doi.org/10.3390/en15207692.

[6] Barbour ER, Pottie DL, Eames P. Why is adiabatic compressed air energy storage yet to become a viable energy storage option? iScience 2021;24(5):102440. http://dx.doi.org/10.1016/j.isci.2021.102440.

[7] Ma S, Wang X, Negnevitsky M, Franklin E. Performance investigation of a wave-driven compressed air energy storage system. J Energy Storage 2023;73:109126. http://dx.doi.org/10.1016/j.est.2023.109126.

[8] Li F, Yu Y, Shu Y, Liu X. Study on characteristics of photovoltaic and photothermal coupling compressed air energy storage system. Process Saf Environ Prot 2023;178:147–55. http://dx.doi.org/10.1016/j.psep.2023.08.033.

[9] Adib M, Nasiri F, Haghighat F. Integrating wind energy and compressed air energy storage for remote communities: A bi-level programming approach. J Energy Storage 2023;72:108496. http://dx.doi.org/10.1016/j.est.2023.108496.

[10] Budt M, Wolf D, Span R, Yan J. A review on compressed air energy storage: Basic principles, past milestones and recent developments. Appl Energy 2016;170:250–68. http://dx.doi.org/10.1016/j.apenergy.2016.02.108.

[11] Barbour ER, Pottie DL. Adiabatic compressed air energy storage technology. Joule 2021;5(8):1914–20. http://dx.doi.org/10.1016/j.joule.2021.07.009.

[12] Hounslow DR, Grindley W, Loughlin RM, Daly J. The development of a combustion system for a 110 MW CAES plant. J Eng Gas Turbines Power 1998;120(4):875–83. http://dx.doi.org/10.1115/1.2818482.

[13] Jafarizadeh H, Soltani M, Nathwani J. Assessment of the Huntorf compressed air energy storage plant performance under enhanced modifications. Energy Convers Manage 2020;209:112662. http://dx.doi.org/10.1016/j.enconman.2020.112662.

[14] Boyce MP. 20 - Gas turbine performance test. In: Boyce MP, editor. Gas turbine engineering handbook (fourth edition). 4th ed.. Oxford: Butterworth-Heinemann; 2012, p. 769–802. http://dx.doi.org/10.1016/B978-0-12-383842-1.00020-2.

[15] Salvini C, Giovannelli A, Farhat H. On the possibility of using an industrial steam turbine as an air expander in a Compressed Air Energy Storage plant. J Energy Storage 2022;55:105453. http://dx.doi.org/10.1016/j.est.2022.105453.

[16] Surywanshi GD, Pillai BBK, Patnaikuni VS, Vooradi R, Anne SB. 4-E analyses of chemical looping combustion based subcritical, supercritical and ultra-supercritical coal-fired power plants. Energy Convers Manage 2019;200:112050. http://dx.doi.org/10.1016/j.enconman.2019.112050.

[17] Holden P, Moen D, DeCorso M, Howard J. Alabama electric cooperative Compressed Air Energy Storage (CAES) plant improvements. In: Turbo expo: Power for land, sea, and air, Volume 3: Heat Transfer; Electric Power; Industrial and Cogeneration, 2000, http://dx.doi.org/10.1115/2000-GT-0595.

[18] Wang S, Zhang X, Yang L, Zhou Y, Wang J. Experimental study of compressed air energy storage system with thermal energy storage. Energy 2016;103:182–91. http://dx.doi.org/10.1016/j.energy.2016.02.125.

[19] Ma L, Zhang X, Zhang Z, Wang Y, Si Y, Chen X, Zhang T, Xue X. Application of the multi-stage centrifugal compressor 1D loss model in the adiabatic compressed air energy storage. Energy Convers Manage 2023;283:116908. http://dx.doi.org/10.1016/j.enconman.2023.116908.

[20] Du R, He Y, Chen H, Xu Y, Li W, Deng J. Performance and economy of trigenerative adiabatic compressed air energy storage system based on multi-parameter analysis. Energy 2022;238:121695. http://dx.doi.org/10.1016/j.energy.2021.121695.

[21] Zhang N, Cai R. Analytical solutions and typical characteristics of part-load performances of single shaft gas turbine and its cogeneration. Energy Convers Manage 2002;43(9):1323–37. http://dx.doi.org/10.1016/S0196-8904(02)00018-3.

[22] Sciacovelli A, Li Y, Chen H, Wu Y, Wang J, Garvey S, Ding Y. Dynamic simulation of Adiabatic Compressed Air Energy Storage (A-CAES) plant with integrated thermal storage – Link between components performance and plant performance. Appl Energy 2017;185:16–28. http://dx.doi.org/10.1016/j.apenergy.2016.10.058.

[23] Pottie D, Cardenas B, Garvey S, Rouse J, Hough E, Bagdanavicius A, Barbour E. Comparative analysis of isochoric and isobaric adiabatic compressed air energy storage. Energies 2023;16(6). http://dx.doi.org/10.3390/en16062646.

[24] Tola V, Meloni V, Spadaccini F, Cau G. Performance assessment of Adiabatic Compressed Air Energy Storage (A-CAES) power plants integrated with packed-bed thermocline storage systems. Energy Convers Manage 2017;151:343–56. http://dx.doi.org/10.1016/j.enconman.2017.08.051.

[25] Dixon SL, Hall CA. Fluid mechanics and thermodynamics of turbomachinery. 7th ed.. Butterworth-Heinemann; 2014, http://dx.doi.org/10.1016/C2011-0-05059-7.

[26] Aungier RH. Axial flow compressors: a strategy for aerodynamic design and analysis. 1st ed.. Wiley–Blackwell; 2003.

[27] Barbour E, Mignard D, Ding Y, Li Y. Adiabatic Compressed Air Energy Storage with packed bed thermal energy storage. Appl Energy 2015;155:804–15. http://dx.doi.org/10.1016/j.apenergy.2015.06.019.

[28] Ran P, Zhang H, Qiao Y, Wang J, Li Z, Wang Y. Thermodynamic analysis for a novel steam injection adiabatic compressed air energy storage hybrid system. J Energy Storage 2022;55:105424. http://dx.doi.org/10.1016/j.est.2022.105424.

[29] Pottie DL. Adiabatic compressed air energy storage: Fundamental efficiency limits based on exergy analysis, key technology outstanding challenges and application oriented axial-flow compressor design and performance prediction (Ph.D. thesis), Loughborough University; 2023.

[30] Bell IH, Wronski J, Quoilin S, Lemort V. Pure and pseudo-pure fluid thermophysical property evaluation and the open-source thermophysical property library CoolProp. Ind Eng Chem Res 2014;53(6):2498–508. http://dx.doi.org/10.1021/ie4033999.

[31] Crotogino F, Mohmeyer K-U, Scharf R. Huntorf CAES: More than 20 years of successful operation. In: Solution mining research institute spring conference. 2001, p. 1–7, Accesses on Jan 30, 2024. Available at http://www.fze.uni-saarland.de/AKE_Archiv/AKE2003H/AKE2003H_Vortraege/AKE2003H03c_Crotogino_ea_HuntorfCAES_CompressedAirEnergyStorage.pdf.

[32] DOW. DOWTHERM a technical data sheet. Datasheet 176-01472-0417, Dow; 2021, Available on: https://www.dow.com/en-us/pdp.dowtherm-a-heat-transfer-fluid.238000z.html#tech-content.

[33] Sarmast S, Rouindej K, Fraser RA, Dusseault MB. Optimizing near-adiabatic compressed air energy storage (NA-CAES) systems: Sizing and design considerations. Appl Energy 2024;357:122465. http://dx.doi.org/10.1016/j.apenergy.2023.122465.

[34] Bailie R, Edmonds R, Salas R. Compressed air energy storage (CAES) : A proven solution for cost-effective, grid-scale and long-duration power storage. White paper, 2021.

[35] Guo W, Zuo Z, Sun J, Hou H, Liang Q, Chen H. Experimental investigation on off-design performance and adjustment strategies of the centrifugal compressor in compressed air energy storage system. J Energy Storage 2021;38:102515. http://dx.doi.org/10.1016/j.est.2021.102515.

[36] Guo H, Xu Y, Zhang Y, Guo C, Sun J, Zhang X, Li W, Chen H. Off-design performance and operation strategy of expansion process in compressed air energy systems. Int J Energy Res 2019;43(1):475–90. http://dx.doi.org/10.1002/er.4284.

[37] Guo H, Xu Y, Zhang Y, Liang Q, Tang H, Zhang X, Zuo Z, Chen H. Off-design performance and an optimal operation strategy for the multistage compression process in adiabatic compressed air energy storage systems. Appl Therm Eng 2019;149:262–74. http://dx.doi.org/10.1016/j.applthermaleng.2018.12.035.

[38] Bai J, Chen W, Xie N, Ma L, Wang Y, Zhang T, Xue X. Dynamic characteristics and optimizations of the proposed combined cold and power system with integrated advanced adiabatic compressed air energy storage and double-effect compression-absorption refrigeration. Energy 2023;283:128474. http://dx.doi.org/10.1016/j.energy.2023.128474.

[39] Chen L, Zhang L, Yang H, Xie M, Ye K. Dynamic simulation of a Re-compressed adiabatic compressed air energy storage (RA-CAES) system. Energy 2022;261:125351. http://dx.doi.org/10.1016/j.energy.2022.125351.

[40] Tournier J-M, El-Genk MS. Axial flow, multi-stage turbine and compressor models. Energy Convers Manage 2010;51(1):16–29. http://dx.doi.org/10.1016/j.enconman.2009.08.005.

[41] Schobeiri MT. Turbomachinery flow physics and dynamic performance. 2nd ed.. Springer; 2012.

[42] Vavra MH. Aero -thermodynamics and flow in turbomachines. 1st ed.. Wiley; 1960.

[43] Cengel YA, Cimbala JM. fluid mechanics: fundamentals and applications. 3rd ed.. McGraw-HIll; 2013.

[44] Horlock JH. Axial flow compressors: fluid mechanics and thermodynaics. 1st ed.. Butterworths Scientific Publications; 1958.

[45] To H-O, Miller RJ. The effect of aspect ratio on compressor performance. J Turbomach 2019;141(8). http://dx.doi.org/10.1115/1.4043219.

[46] Yaras MI, Sjolander SA. Prediction of tip-leakage losses in axial turbines. J Turbomach 1992;114(1):204–10. http://dx.doi.org/10.1115/1.2927987.
[47] Lieblein S, Roudebush WH. Theoretical loss relations for low-speed two-dimensional-cascade flow. Technical note 3662, National Advisory Committee for Aeronautics; 1956.
[48] Horlock JH. The determination of end-wall blockage in axial compressors: A comparison between various approaches. J Turbomach 1999;122(2):218–24. http://dx.doi.org/10.1115/1.555452.
[49] Koch CC, Smith Jr LH. Loss sources and magnitudes in axial-flow compressors. J Eng Power 1976;98(3):411–24. http://dx.doi.org/10.1115/1.3446202.
[50] LIU B, ZHANG C, AN G, FU D, YU X. Using tandem blades to break loading limit of highly loaded axial compressors. Chin J Aeronaut 2022;35(4):165–75. http://dx.doi.org/10.1016/j.cja.2021.07.031.
[51] Mohsen M, Owis FM, Hashim AA. The impact of tandem rotor blades on the performance of transonic axial compressors. Aerosp Sci Technol 2017;67:237–48. http://dx.doi.org/10.1016/j.ast.2017.04.019.
[52] Ghazanfari B, Nili-Ahmadabadi M, Torabi-Farsani A, Noorsalehi MH. Numerical study of camber and stagger angle effects on the aerodynamic performance of tandem-blade cascades. Propuls Power Res 2018;7(1):30–42. http://dx.doi.org/10.1016/j.jppr.2018.02.003.
[53] Moran J. An introduction to theoretical and computational aerodynamics. Dover books on aeronautical engineering, 1st ed.. Dover Publications; 2003.
[54] Lieblein S. Loss and stall analysis of compressor cascades. J Basic Eng 1959;81(3):387–97. http://dx.doi.org/10.1115/1.4008481.
[55] Lieblein S. Analysis of experimental low-speed loss and stall characteristics of two-dimensional compressor blade cascades. Report NACA-RM-E57A28, NACA; 1957.
[56] Howell AR. Fluid dynamics of axial compressors. Proc Inst Mech Eng 1945;153(1):441–52. http://dx.doi.org/10.1243/PIME_PROC_1945_153_049_02.
[57] Mathworks. Piecewise cubic Hermite interpolating polynomial. 2023, URL https://uk.mathworks.com/help/matlab/ref/pchip.html, Accessed on May 16th, 2023.
[58] Axial and centrifugal compressors and expander-compressors for petroleum, chemical and gas industry services. 2022.
[59] Petroleium, petrochemical and natural gas industries - axial and centrifugal compressors and expander-compressors. 2015.
[60] Grazzini G, Milazzo A. Thermodynamic analysis of CAES/TES systems for renewable energy plants. Renew Energy 2008;33(9):1998–2006. http://dx.doi.org/10.1016/j.renene.2007.12.003.